Nano Research Energy

ISSN 2791-0091 (print); 2790-8119 (online)
https://doi.org/10.26599/NRE.2023.9120051

Review Article

Borophene-based materials for energy, sensors and information storage applications

Chuang Hou, Guoan Tai (✉), Yi Liu, Zitong Wu, Xinchao Liang, and Xiang Liu

The State Key Laboratory of Mechanics and Control of Mechanical Structures and Laboratory of Intelligent Nano Materials and Devices of Ministry of Education, College of Aerospace Engineering, Nanjing University of Aeronautics and Astronautics, Nanjing 210016, China

Received: 27 November 2022 / **Revised:** 27 December 2022 / **Accepted:** 28 December 2022

ABSTRACT

Borophene, as a rising-star monoelemental two-dimensional (2D) material, has motivated great interest because of its novel properties, such as anisotropic plasmonics, high carrier mobility, mechanical compliance, optical transparency, ultrahigh thermal conductance, and superconductivity. These properties make it an ideal candidate for use in the field of energy, sensors, and information storage. Stimulated by the realization of pioneering experimental works in 2015 and the follow-up synthesis experiments, a series of high-performance borophene-based devices in the fields, including supercapacitors, batteries, hydroelectric generators, humidity sensors, gas sensors, pressure sensors, and memories, have been experimentally reported in recent years, which are beneficial to the transition of borophene-based materials from experimental synthesis to practical application. Therefore, in addition to paying attention to the experimental preparation of borophene, significant efforts are needed to promote the advancement of related applications of borophene. In this review, after providing a brief overview of borophene evolution and synthesis, we mainly summarize the applications of borophene-based materials in energy storage, energy conversion, energy harvesting, sensors, and information storage. Finally, based on the current research status, some rational suggestions and discussions on the issues and challenges in the future research direction are proposed.

KEYWORDS

borophene, energy, energy storage, energy conversion, sensors, information storage

1 Introduction

Owing to their special and novel physical and chemical properties, two-dimensional (2D) materials, such as graphene [1–3], 2D metal carbides and nitrides (MXenes) [4–7], transition metal dichalcogenides (TMDs) [8, 9], hexagonal boron nitride (h-BN) [10, 11] and black phosphorus (BP) [12–15], have been noted to play promising roles in a variety of fields of basic science and advanced technology. Driven by the gradually mature preparation method, these 2D materials have also shown great application potential in various fields such as sensors, biomedicine, optoelectronics, and energy storage. However, the potential application still suffers from challenges and issues because of its intrinsic limitations or shortcomings. Despite graphene or MXenes possesses high carrier mobility and excellent mechanical strength, the zero bandgap character seriously restricts its application in field effect transistors (FETs) and optical sensing devices [2]. As a kind of multivariate 2D material, layered TMDs family has been proven to have a finite bandgap, but low carrier mobility limits its development in sensing fields [9]. As a typical graphene-like layered material, 2D h-BN exhibits a wide band gap of up to 5 eV [11], which suggests that it has great potential as an insulating or sealing layer of semiconductor devices. BP, as the most stable allotrope of phosphorus, is a typical thickness-dependent direct bandgap layered material and has a high hole mobility of ~ 1,000 $cm^2/(V{\cdot}s)$ in the few-layered structure [12, 13]. The results seem to indicate that BP can be regarded as an omnipotent material. However, few-layered BP shows structure instability under ambient conditions, which is unfavorable to its practical applications. Therefore, an alternative novel 2D material is urgently required. Monoelemental 2D materials are expected to be considered as excellent candidates due to their structural simplicity and doping controllability [16–20].

Borophene [21], as rising-star monoelemental 2D material, has motivated great interest due to its novel properties, such as anisotropic plasmonics, mechanical compliance, optical transparency, ultrahigh thermal conductance and superconductivity [21–35]. Additionally, it has been predicted that borophene has some more excellent properties than the above-mentioned 2D materials. Various structural phases of borophene endow

© The Author(s) 2023. Published by Tsinghua University Press. The articles published in this open access journal are distributed under the terms of the Creative Commons Attribution 4.0 International License (http://creativecommons.org/licenses/by/4.0/), which permits use, distribution and reproduction in any medium, provided the original work is properly cited.

Address correspondence to Guoan Tai, taiguoan@nuaa.edu.cn

them have an optional wide bandgap range [22–24, 36], which shows great potential in bridging the space between semi-metallic zero-bandgap graphene, large-bandgap TMDs, and insulating h-BN. Compared to few-layered BP, some typical borophenes have shown good stability in the ambient environment or even in acid or base solvents [27, 37–41], which may compensate for the poor stability of few-layered BP. In addition, it has been predicted that borophene is expected to become an advancing electrode material for rechargeable lithium-ion or sodium-ion batteries, which display higher storage capacities than those of graphene [42, 43]. Furthermore, it was reported that the 8B-Pmmn borophene possessed ultrahigh predicted carrier mobility of 10^6 $cm^2/(V·s)$ at room temperature [44], which was even higher than that in graphene (15,000 $cm^2/(V·s)$) [3]. The electron and hole mobility of semiconducting α'-sheet was respectively predicted to be as high as approximately 20,000 and 1,500 $cm^2/(V·s)$ [45], which are higher than those of monolayer BP (~ 1,000 $cm^2/(V·s)$) [14]. Many theoretical works have pointed out that there is a significant atomic bonding between boron atoms and gas molecules and rapid charge transfer from gas molecules to the surface of borophene [46–49]. Besides, it was also demonstrated that borophene had a large number of active sites and the calculated value of its hydrogen adsorption free energy (ΔG_H) was even close to zero [50, 51]. Based on these intriguing properties, borophene seems to be suitable for many fields such as energy and sensors as well as information storage. Due to the experimental realization of the stable and high-quality borophenes and their heterostructures in recent years [27, 37–41, 52–61], numerous research works for their applications in the three fields have been experimentally reported [37–41, 52–71].

To date, some literature reviews have been published, including the developments of borophene structures, synthesis, properties, and potential applications [23–26]. Nevertheless, most reviews have discussed the potential applications from a theoretical perspective and few reviews have devoted much attention to comprehensively covering the experimental developments of borophene-based materials for application fields, especially energy, sensors, and information storage. In this review, after a brief introduction of borophene evolution and synthesis, we systematically conclude the recent experimental works on borophene-based materials applications in the specific three fields (Fig. 1). Finally, we summarize the status of borophene-based applications and propose some rational suggestions and discussions on the issues and challenges in the future research direction.

2 Borophene evolution and synthesis

Although borophene has realized continuous breakthroughs in theories and experiments, its related research started relatively late because of the complexity of its structure and the lack of the corresponding bulk counterpart. Theoretically, according to Aufbau principle, it was not until 1997 that Boustani et al. reported stable 2D boron sheets which could be constructed from the pentagonal and hexagonal pyramids [72]. Subsequently, a variety of 2D boron sheets with different buckling triangular patterns have been demonstrated to be more stable. To further improve the stability of 2D boron, Szwacki et al. discovered that the C_{60}-like B_{80} buckyball could be expanded to form a novel 2D boron structure (α-sheet) [73] and the formation of hexagonal holes within the triangular sheet could provide stronger cohesive energy [74, 75]. Afterwards, numerous 2D boron structures with different hexagonal hole arrangements have been predicted in theoretical works, including β-sheet, $g_{1/8}$-sheet, $g_{2/15}$-sheet, and so on [76–78]. In 2012, Wu et al. investigated a series of highly stable novel boron monolayer

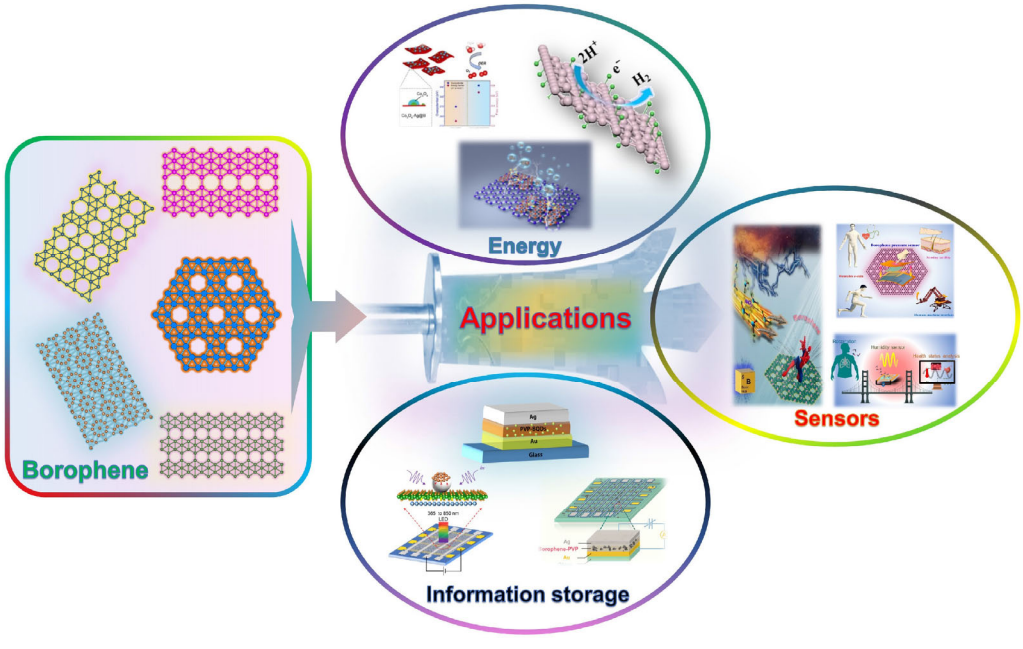

Figure 1 Multifunctional applications of borophene-based materials in the fields of energy, sensors, and information storage. Energy: Reproduced with permission from Ref. [41], © American Chemical Society 2021. Reproduced with permission from Ref. [62], © American Chemical Society 2021. Reproduced with permission from Ref. [67], © Elsevier B.V. 2021. Sensors: Reproduced with permission from Ref. [58], © The Royal Society of Chemistry 2021. Reproduced with permission from Ref. [69], © Elsevier Ltd. 2022. Information storage: Reproduced with permission from Ref. [37], © Wiley-VCH Verlag GmbH & Co. KGaA, Weinheim 2020. Reproduced with permission from Ref. [140], © American Chemical Society 2020. Reproduced with permission from Ref. [60], © Tsinghua University Press 2022.

sheets and revealed that α_1-sheet and β_1-sheet were more stable than α-sheet, which provided a new idea for exploring the 2D boron polymorphs [36].

To further guide the experimental realization of stable 2D boron sheets, an increasing number of effective strategies have been proposed theoretically, such as substrates support, surface passivation, and layer stacking [36, 78–85]. For substrate support, typically, in 2013, Liu et al. explored the possibility of growing the 2D boron sheets on Au (111), Ag (111), Cu (111), MgB_2, and TiB_2 surfaces [78]. Consequently, Zhang et al. using the cluster-expansion method based on first-principles calculations and surface structure search, systematically predicted the stable 2D boron structures on Au, Ag, Cu, and Ni metal substrates [79]. The results indicated that the metal substrates could facilitate the nucleation of 2D boron structures and provide extra electrons to stabilize them. Besides, it was also revealed that different metal substrates could give rise to the formation of 2D boron structures with different phases, which were confirmed by subsequent synthesis experiments [28, 29]. In 2019, Zhang et al. also identified the edges of borophene on Ag and further unveiled the growth mechanism of the edges morphology and island shape [80]. Surface passivation has been considered as another effective strategy to stabilize the structure of borophene, modify its surface and open its band gap [36, 81–84]. It is worth noting that our group has reported a series of stable hydrogenated borophene (HB) with α' phase in which some of them have semiconductor properties, which have been confirmed by experiments later. In 2022, Xu et al. theoretically confirmed that hydrogenation could further improve the stability of borophene and determined structures of hydrogenated borophene polymorphs on Ag (111) [84]. Subsequently, they also predicted a highly stable, semiconducting, and quasi-freestanding bilayer borophene on Ag (111) by an extensive structure search based on first-principles calculations [85].

Compared with theoretical works on borophene, its experiments on how to synthesize borophene have lagged behind for a long time. Until 2014, based on the experimental investigation of typical planar boron clusters, named B_{36}, the concept of borophene was first proposed. In 2015, our group first reported the crystalline and stable monolayer boron sheets (γ-B_{28}) synthesized by a home-made two-zone chemical deposition vapor (CVD) method [27]. In addition, the sheets were demonstrated to be a semiconductor with an optical band gap of 2.25 eV. Afterwards, Guisinger and coworkers experimentally realized borophenes with different phases, which could be obtained by controlling the boron deposition rate on a cleaned Ag surface via molecular beam epitaxy (MBE) method [28]. Meanwhile, Feng and coworkers synthesized the borophene islands with a width of only tens of nanometers by means of the basically same way [29]. The three experimental works are regarded as pioneering experimental breakthroughs for borophene. After these, the synthesis of crystalline borophenes with various structure phases has been successively achieved on some typical metal and even insulate surfaces through CVD and MBE methods [38–41, 86–90]. However, the structural instability of borophene in air has always been a recognized and urgent problem in the field of borophene, which limits the experimental verification of its novel properties and potential applications.

To solve the problem and advance the field, some stable borophene-based materials, such as hydrogenated borophene [37, 91–94], borophene-based heterostructures [57–60, 95, 96], and bilayer borophene [97, 98], have been reported experimentally. In 2020, our group first proposed a simple *in-situ* thermal decomposition method to prepare ultrastable, semiconducting, and high-quality hydrogenated borophene by using the sodium borohydride as boron source in a hydrogen-rich environment [37]. Furthermore, some typical borophene-based heterostructures, such as borophene–graphene [57], borophene–MoS_2 [58], and borophene–ZnO [59, 60], were successfully prepared. Moreover, Liu et al. have synthesized borophene-graphene heterostructures on graphene by using MBE method [95]. In 2021, Li et al. synthesized hydrogenated borophene polymorphs by hydrogenating pre-synthesized borophene in ultrahigh vacuum environment [94]. Different from the pristine borophene with instantaneous oxidation characteristics, the hydrogenated borophene showed negligible oxidation in air. Recently, Liu et al. [97] and Chen et al. [98] from two independent groups respectively reported the successful synthesis of two types of bilayer borophene on Ag (111) and Cu (111) surfaces, which were prone to being more stable than their monolayer structures. Besides, although borophene has no corresponding bulk counterpart, it has been demonstrated that it can be prepared by liquid phase exfoliation method [52–54, 66]. The above typical borophene research works are chronologically illustrated in Fig. 2. The borophene evolution and synthesis have stimulated the experimental developments of borophene-based materials in the fields of energy, sensors, and information storage.

3 Borophene-based materials for energy

3.1 Borophene-based materials for energy storage

Energy storage-related devices, such as supercapacitors, lithium-metal batteries, and lithium-sulfur batteries, have attracted much attention due to their high energy efficiency, good portability, and environmental friendliness [99–105]. 2D materials with large specific surface area, a large number of active sites and strong chemical stability have been considered to be exploited in these devices. However, some typical 2D materials have displayed their intrinsic shortcomings. For example, the quantum capacitance effect in graphene has limited the total specific capacity (sCap) of its supercapacitor [106]. Although good catalytic activities have been found in lithium-sulfur (Li-S) batteries based on graphene, black phosphorene and MXene, slow charge/discharge rate, poor cycle stability, and low capacity have limited practical requirements of industrial applications [107–109]. Therefore, exploration of novel 2D materials with highly efficient adsorption, large catalytic activity, and long-time stability is necessary for the future development of energy storage-related devices.

Borophene, as a novel promising 2D material, has been predicted to have a high theoretical capacity of ~ 1,860 mAh/g, which is superior to that of other typical 2D materials [42]. In addition, borophene with a diversity of bonding modes and rich polymorphs shows strong bonding energy to polysulfide clusters [110–112]. The excellent performances have been experimentally demonstrated in energy storage devices based on borophene in recent years.

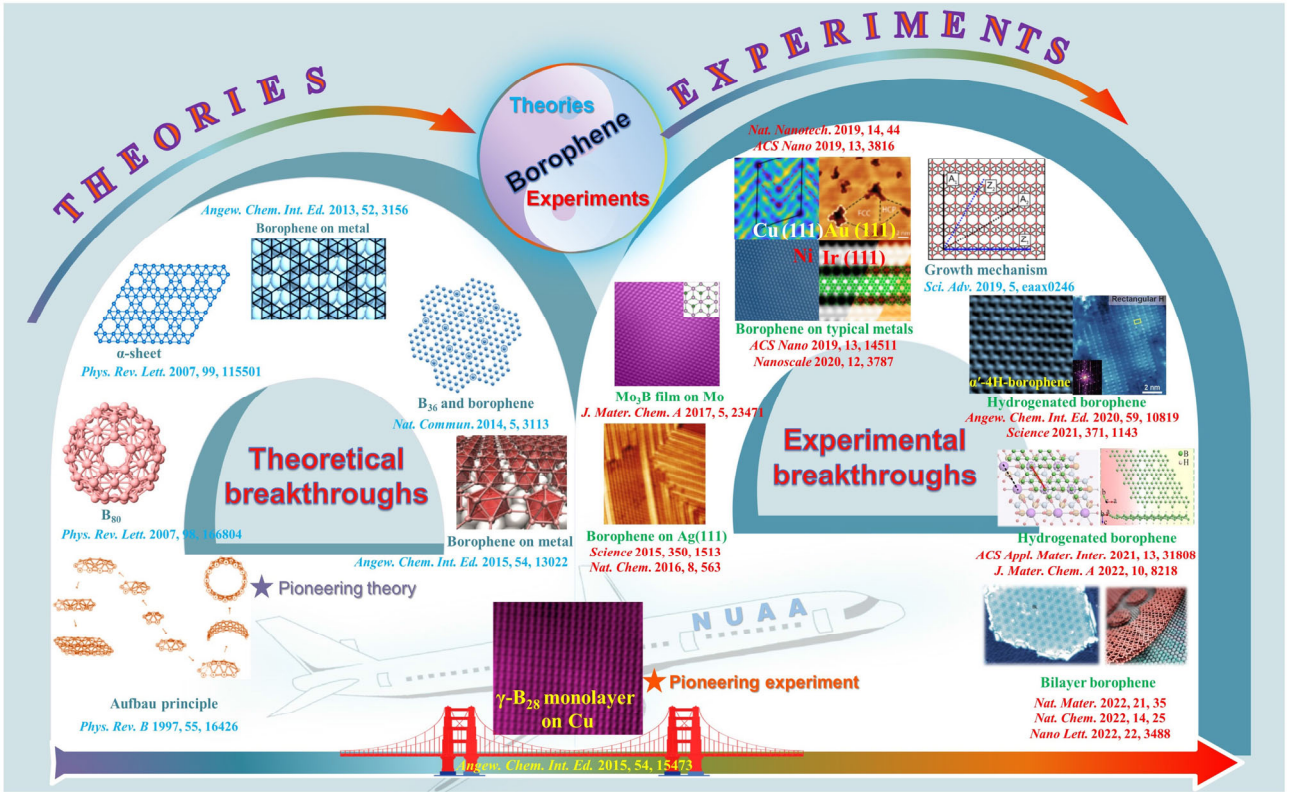

Figure 2 Major breakthroughs for the evolution and synthesis of borophene. Reproduced with permission from Ref. [72], © The American Physical Society 1997. Reproduced with permission from Ref. [73], © The American Physical Society 2007. Reproduced with permission from Ref. [77], © Wiley-VCH Verlag GmbH & Co. KGaA, Weinheim 2013. Reproduced with permission from Ref. [21], © Nature Publishing Group, a division of Macmillan Publishers Limited 2014. Reproduced with permission from Ref. [79], © Wiley-VCH Verlag GmbH & Co. KGaA, Weinheim 2015. Reproduced with permission from Ref. [27], © Wiley-VCH Verlag GmbH & Co. KGaA, Weinheim 2015. Reproduced with permission from Ref. [28], © American Association for the Advancement of Science 2015. Reproduced with permission from Ref. [64], © The Royal Society of Chemistry 2017. Reproduced with permission from Ref. [87], © Wu, R. T. et al, under exclusive licence to Springer Nature Limited 2018. Reproduced with permission from Ref. [88], © American Chemical Society 2019. Reproduced with permission from Ref. [89], © American Chemical Society 2019. Reproduced with permission from Ref. [38], © The Royal Society of Chemistry 2020. Reproduced with permission from Ref. [80], © Zhang, Z. H. et al. 2019. Reproduced with permission from Ref. [37], © Wiley-VCH Verlag GmbH & Co. KGaA, Weinheim 2020. Reproduced with permission from Ref. [94], © Li, Q. C. et al., some rights reserved; exclusive licensee American Association for the Advancement of Science 2021. Reproduced with permission from Ref. [39], © American Chemical Society 2021. Reproduced with permission from Ref. [40], © The Royal Society of Chemistry 2022. Reproduced with permission from Ref. [97], © Liu, X. L. et al., under exclusive licence to Springer Nature Limited 2021. Reproduced with permission from Ref. [85], © American Chemical Society 2022.

Teo and co-workers prepared high-quality few-layer boron sheets by sonication-assisted liquid-phase exfoliation method and fabricated a high-performance supercapacitor using the boron sheets as the electrode material [52]. SEM results show that the obtained boron sheets are almost transparent and have a thinner thickness than that of the bulk boron, which demonstrates the successful preparation of the boron sheets (Figs. 3(a)–3(c)). In addition, the boron sheets dispersions with light-brown color show good stability and dispersion (Figs. 3(b) and 3(c)), which indicates the formation of the structurally stable boron sheets.

The obtained boron sheets have shown great potential in the field of energy storage. As shown in Fig. 3(d), the electrode of the supercapacitor has an excellent capacitive performance with a stable voltage window. Additionally, the specific capacity would substantially increase with the increase of the voltage window (Fig. 3(d)). Moreover, analysis results of the tested cyclic voltammetry (CV) curves demonstrated that the boron sheets had an outstanding capacitive behavior and showed a fast charge/discharge capacity (Fig. 3(e)).

The galvanostatic charge/discharge tests further reveal that the supercapacitor possesses a relatively small equivalent series resistance (Fig. 3(f)). Figure 3(g) shows the calculated specific capacitances and area-normalized cell capacitances of the supercapacitor at various current densities. The results demonstrated that the maximum specific capacitance of the supercapacitor was obviously superior to that of bulk boron and other typical nanomaterials, such as porous carbon [113] and reduced graphene sheets [114]. Figure 3(h) shows that the supercapacitor has an excellent cycling stability, which is an important prerequisite for the practical application. The excellent electrochemical performances make the supercapacitor based on boron sheets have great potential for its practical application. To further evaluate the potential, the supercapacitor was used to drive a red light-emitting diode (LED) light after charging. Thus, the results demonstrate that the boron sheets have a promising prospect in the design and fabrication of high-performance energy storage devices.

Recently, Abdi et al. reported a new supercapacitor based on borophene sheets, which were synthesized on Si wafer substrate by Al-assisted CVD method [55]. The morphology and topography of the borophene were investigated by field

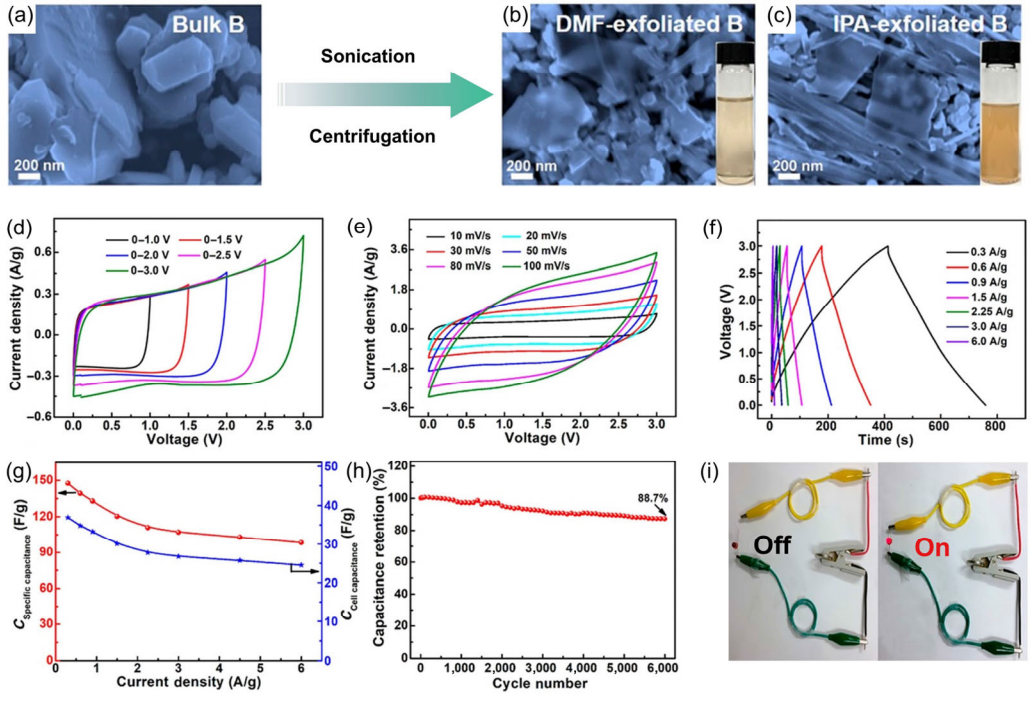

Figure 3 Morphological characterization and electrochemical properties of the supercapacitor based on exfoliated boron sheets. (a)–(c) SEM images of (a) bulk boron and the thin boron sheets exfoliated in (b) N,N-dimethylformamide (DMF) and (c) isopropanol (IPA) solvents. (d) CV curves under different voltage windows at a fixed scan rate of 10 mV/s. (e) CV curves at the scan rates from 10 to 100 mV/s. (f) Galvanostatic charge/discharge curves at different current densities. (g) Calculated specific capacitances and area-normalized cell capacitances of the supercapacitor at various current densities. (h) Cycling stability of the supercapacitor. (i) Photograph of the obtained supercapacitor driving one red LED light. Reproduced with permission from Ref. [52], ©American Chemical Society 2018.

emission scanning electron microscope (FESEM), as shown in Fig. 4(a). It was observed that borophene sheets and Al islands could be clearly distinguished by the brightness of the color. The borophene sheets display a gray color and the Al island locates at the bright zones. In addition, the borophene domains with polygon shape indicates that the sheet has the characteristic of long-range ordered crystal structure. Moreover, because of the high quality of the sheets and good integrity after transferring them on other functional substrates, a high-effective borophene-based supercapacitor was successfully fabricated. The detailed fabrication process of the supercapacitor is displayed in Fig. 4(b).

Electrochemical properties of the pristine graphoil and graphoil/borophene supercapacitor were investigated and compared in Figs. 4(c) and 4(d). It can be found that the borophene-coated supercapacitor has a larger current density–voltage (J–V) curve area than that of the pristine graphoil, which indicates the higher sCap in the borophene-based supercapacitor. Additionally, Fig. 4(e) shows that the electrodes coated by borophene sheets have a high capacitance of 0.75 F/g (350 mF/cm^2), which is significantly higher than that of the ones without borophene (117 mF/cm^2; 0.25 F/g). Because the weight of the coated borophene on graphoil was controlled below 1 mg under all test conditions, the sCap of the borophene was calculated up to up to 350 mF/cm^2. Moreover, a capacitance as high as about 0.58 F/g (270 mF/cm^2) was found at a scan rate of 5 mV/s and decreased with the increase of the scan rate (Fig. 4(f)). Therefore, the high sCap of the borophene-based supercapacitor, which is higher than that of the reported boron-based materials and other typical 2D materials including graphene [113, 114], shows a great potential in the field of energy storage.

As another important energy storage device, batteries have become an indispensable part of various fields, such as medical, transportation, and communications [115]. Due to the rapid progress of these fields, it is urgent to exploit higher energy density, lower cost, and safer batteries. Li-S battery, as a promising candidate, has been regarded as a new generation of energy storage device because of its low cost, environmental friendliness, high specific capacity, and higher energy density than that of lithium-ion battery [110]. Borophene is regarded as an excellent electrode material in lithium-sulfur batteries, which has been systematically verified in recent experiment [62].

Lin et al. developed a low-temperature liquid phase exfoliation method to prepare freestanding crystalline few-layer borophene and then constructed a novel Li-S battery by using the borophene as electrocatalysts and polysulfide immobilizers [62]. Figure 5(a) shows the preparation process of the exfoliated borophene samples. Large-scale borophene sheets could be obtained by selecting the suitable sonication power in N-methyl pyrrolidone (NMP) exfoliated solvent. SEM result shows that the sheets with a smooth and transparent appearance have the lateral size of 2–5 μm (Fig. 5(b)). Furthermore, a typical atomic force microscope (AFM) image shows that the averaged thickness of the sheets is less than 2.32 nm (Fig. 5(c)), which indicates that the sheets are an ultrathin two-dimensional structure.

After the experimental realization of the borophene sheets, they loaded the borophene on carbon nanotubes (CNT) to form CNT/borophene (CNT/B) as highly effective polysulfide electrocatalysts for advanced Li-S battery. Figure 5(d) shows the CV curves of the battery based on CNT/B electrocatalysts at a fixed scan rate of 0.1 mV/s. It can be found that the curves

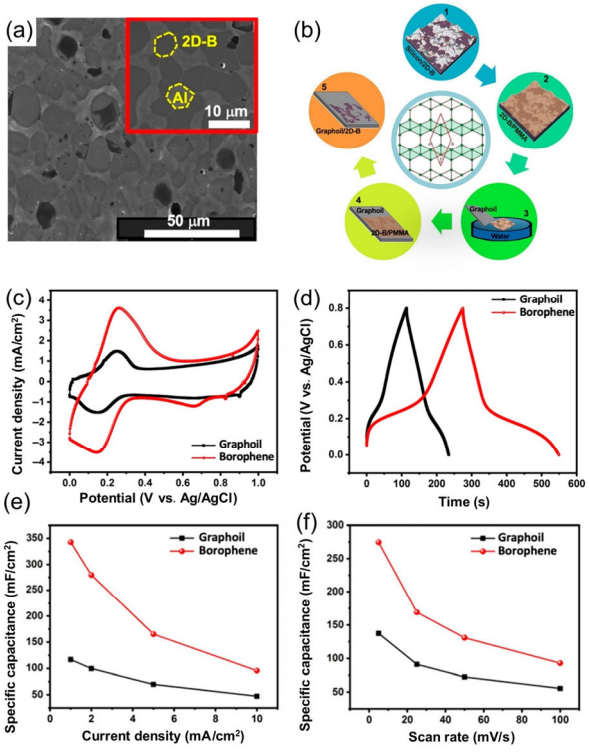

Figure 4 Characterization of borophene and fabrication and electrochemical properties of borophene-based supercapacitor. (a) Field emission scanning electron microscope images of the borophene sheets on the Al substrate. (b) Schematic illustration of fabricating the borophene supercapacitors. The crystal structure of the borophene is shown in the center. (c) CV curves of the borophene supercapacitor at different scan rates. (d) Galvanostatic charge/discharge curves at different current densities. (e) sCap of the pristine graphoil supercapacitor and the one coated with borophene at different current densities. (f) sCap of the pristine graphoil supercapacitor and the one coated with borophene at different scan rates. Reproduced with permission from Ref. [55], ©American Chemical Society 2022.

overlap each other and display good reversibility during the redox process, which demonstrates the high utilization of sulfur. Based on the analysis of Galvanostatic charge/discharge curves, it was observed that the high reversible specific capacities of 919, 993, 1,057, 1,159, 1,236, and 1,329 mAh/g were respectively obtained at 5, 3, 2, 1, 0.5, and 0.3 C rates in the battery (Fig. 5(e)). In addition, the battery could even retain a high capacity of 721 mAh/g at a high current density of 8 C (Fig. 5(f)). Impressively, the battery was able to realize almost complete recovery when the current density backed from 8 to 0.3 C. By contrast, the CNT-based battery had a low capacity of 980 mAh/g at a low current density of 0.3 C and an obvious degradation after a high rate test. Figure 5(g) shows that the CNT/B-based battery has a polarization voltage of 188 mV, which is much lower than that of the CNT-based battery (217 mV). The result indicates that the borophene has high catalytic performance for polysulfide conversion.

Good cycling stability, as a key performance indicator, is necessary for the practical application of batteries. Figure 5(h) shows the long-term cyclic stability test of the CNT/B cathode at a low current density of 0.5 C. It could be found that the capacity of the CNT/B-based battery had almost no degradation and its Coulombic efficiency almost remained at 100% after 300 cycles, which was significantly better than the results of the CNT-based battery. Moreover, high sulfur loads of 5.3 and 7.8 mg/cm^2 with low electrolyte to sulfur ratios (E/S) of 9.8 and 6.8 μL/mg were respectively used in the batteries to reflect their excellent energy density performances (Fig. 5(i)). It was found that the corresponding areal capacities of the batteries could reach about 4.6 and 5.2 mAh/cm^2 when the capacities respectively utilized approximately 870 and 660 mAh/g, which were better than that of the commercial Li-ion batteries (~ 4.0 mAh/cm^2). Besides, the reversible capacity of the CNT/B-based battery still preserved high level with almost no decrease and had a relatively low capacity decay rate after 1,000 cycles (Fig. 5(j)), which indicated its excellent long-term cycling stability.

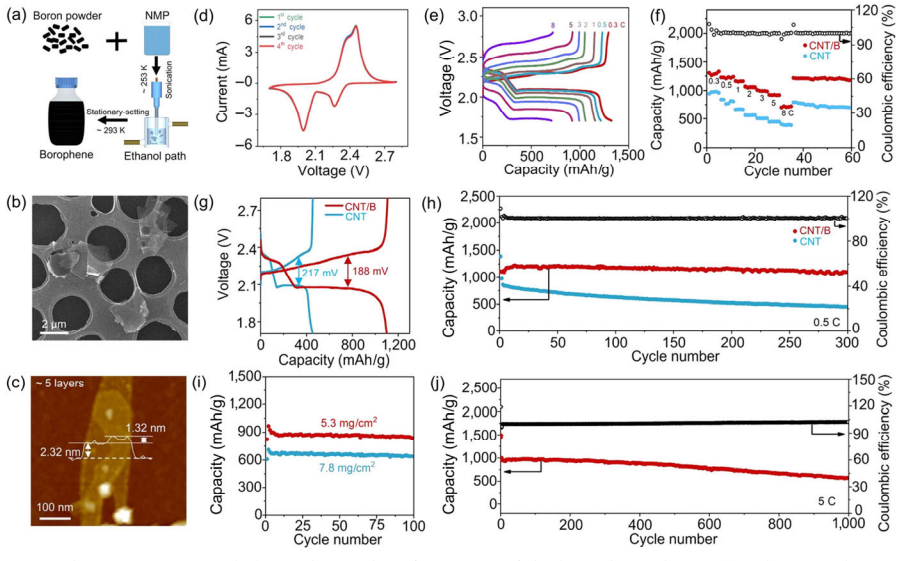

Figure 5 Preparation process, characterization, and electrochemical performances of the borophene sheets. (a) Schematic diagram of the low-temperature liquid phase exfoliation process of the borophene sheets. (b) SEM image of the sheets. (c) AFM image of the sheets. (d) CV curves of the Li-S battery based on CNT/B at a fixed scan rate of 0.1 mV/s. (e) Galvanostatic charge/discharge curves of the CNT/B-based battery at different rates. (f) Rate performances of the batteries based on pristine CNT and CNT/B cathodes. (g) Galvanostatic charge/discharge curves at a current density of 0.5 C. (h) Long-term cyclic stability and Coulombic efficiency of the batteries based on pristine CNT and CNT/B at a current density of 0.5 C, respectively. (i) Cycling tests for the CNT/B-based Li-S batteries with sulfur (S) loadings of 5.3 and 7.8 mg/cm^2 at a current density of 0.3 C. (j) Long-term cyclic stability and Coulombic efficiency of the CNT/B-based batteries at a current density of 0.5 C. Reproduced with permission from Ref. [62], ©American Chemical Society 2021.

Because of the good structure stability and large specific surface area of hydrogenated borophene [37], it was expected to be considered as promising nanofillers to improve the performances of polymer-based solid-state electrolytes for lithium metal batteries. Recently, Liu et al. have successfully used HB as functional nanofillers for the quasi-solid-state electrolyte based on polyethylene oxide (PEO) [63]. It was noted that the HB was prepared by *in-situ* thermal decomposition method, which was detailedly reported in our previous works [37]. The HB-based quasi-solid-state electrolytes could be fabricated by a traditional method, which were composed of the HB sheets, ionic liquids (1-ethyl-3-methylimidazolium bis(trifluoromethylsulfonyl)imide (EMIM-TFSI)), PEO, and bis(trifluoromethane)sulfoni mide lithium salt (Li TFSI). The detailed fabrication process is shown in Fig. 6(a). Then, the Li/composite polymer electrolytes (CPEs)/Li symmetrical cells were further constructed to evaluate the electrochemical performance (Figs. 6(c)–6(f)). Figure 6(c) shows the galvanostatic charge/discharge curves of the 3 wt.% HB-PEO electrolyte at 60 °C. It could be observed that the specific capacity of 140 mAh/g degraded only 6% after 100 cycles at a low current density of 0.1 C rate. Moreover, the full-cell based on the electrolyte had a flat and tight interface and showed a low voltage hysteresis of about 210 mV (Fig. 6(d)), indicating that the HB sheets could accelerate the transfer rate of Li ions. To investigate the cycling stability at various current densities, the rate performances of the full-cell based on HB-PEO electrolyte were also tested. It was observed that the capacities could be up to 35, 71, 97, and 115 mAh/g at 5, 2, 1, and 0.5 C rates, respectively (Figs. 6(e) and 6(f)). The results prove that the hydrogenated borophene can be viewed as a promising nanofiller to improve the performance of lithium metal batteries.

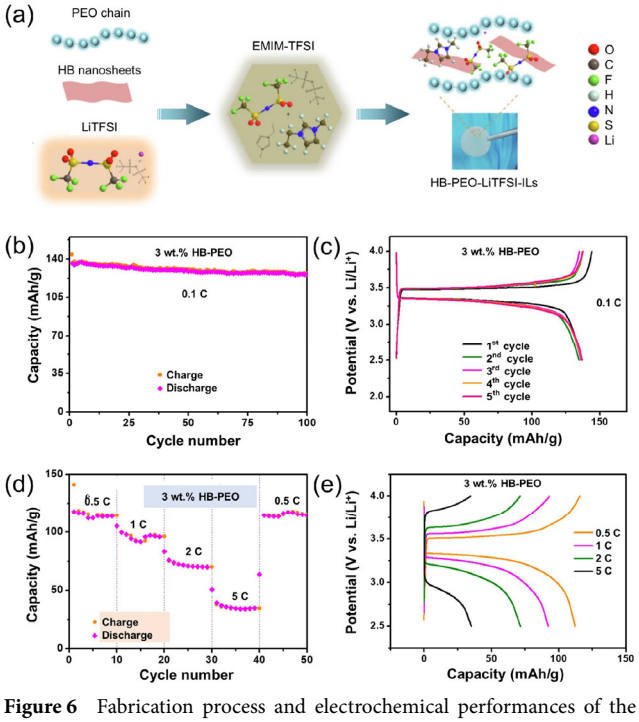

Figure 6 Fabrication process and electrochemical performances of the HB-based quasi-solid-state electrolyte. (a) Schematic diagram of the fabrication process of the HB-based electrolyte. (b) Cycling stability of the 3 wt.% HB-PEO quasi-solid-state electrolyte at 0.1 C rate. (c) Galvanostatic charge/discharge curves of the electrolyte. (d) Rate performances of the electrolyte. (e) Galvanostatic charge/discharge curves of the electrolyte at different rates. Reproduced with permission from Ref. [63], © Elsevier Inc. 2022.

3.2 Borophene-based materials for energy conversion

Apart from the promising prospect of borophene in energy storage, it has also shown great potential for energy conversion. For example, borophene has been theoretically proven to be excellent catalysts for hydrogen evolution reaction (HER) and oxygen evolution reaction (OER), which can be attributed to a large number of active sites on its surface [51, 116–119]. In addition, its calculated free energy of hydrogen adsorption (ΔG_H) in HER was even close to zero [50, 51]. Although it was also predicted that the choice of the conductive substrates could affect the HER or OER activity of borophene, it still retained a high catalytic activity by selecting the appropriate supported substrate [116–118]. Therefore, many related experiments have been reported to promote the development of the field in recent years.

Although borophene has been predicted to have excellent electrocatalytic performances, the corresponding experiments have not been followed immediately after the three pioneering works for experimental synthesis. It can be attributed to the poor stability of its structure. To promote the development of the boron-based materials and provide the guidance for borophene-based applications in energy conversion, our group reported the preparation of two-dimensional Mo_3B films with large-area and high-quality after the experimental realization of borophene and explored its HER activity [64]. The films were synthesized on clean Mo foils at 900 °C in a H_2-rich environment by chemical vapor deposition (CVD) method (Fig. 7(a)). A typical high-resolution transmission electron

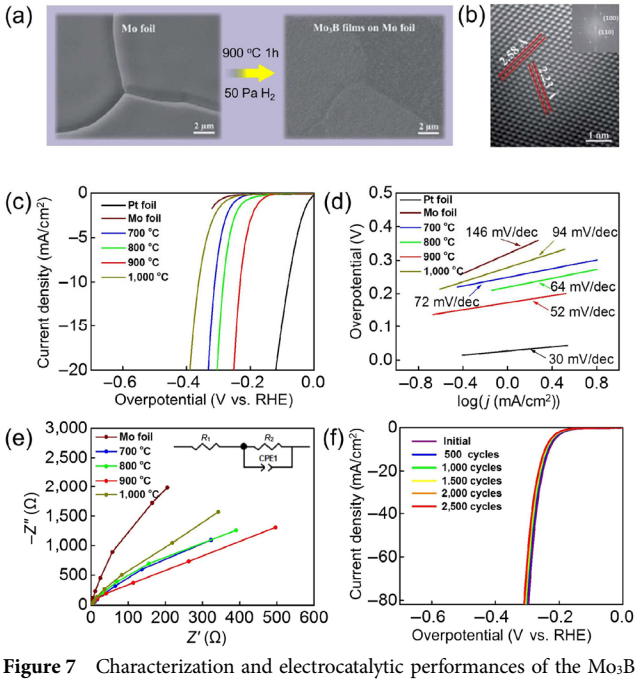

Figure 7 Characterization and electrocatalytic performances of the Mo_3B films. (a) SEM images of the Mo foil (left) and Mo_3B films grown on the Mo foil (right). (b) HRTEM image of the Mo_3B films. (c) and (d) *IR*-corrected LSV curves (c) and the corresponding Tafel plots (d) of the samples grown at different temperatures. A standard commercial Pt electrode and pure Mo foil were selected as control experiments. (e) EIS Nyquist plots of the pure Mo foil and the samples synthesized at different temperatures. (f) Cycling stability tests of the Mo_3B films obtained at 900 °C for 60 min. Reproduced with permission from Ref. [64], © The Royal Society of Chemistry 2017.

microscope (HRTEM) image indicates that the film has a good crystallinity and its crystal structure corresponds to that of the rhombohedral Mo_3B (Fig. 7(b)).

The electrocatalytic HER performances of the Mo_3B films were evaluated in 0.5 M H_2SO_4 electrolyte using a standard three-electrode system. Figure 7(c) shows the results of linear sweep voltammetry (LSV) at a fixed scan rate of 5 mV/s. It was noted that the Mo_3B films grown at 900 °C (Mo_3B-900) showed higher electrocatalytic activity than pure Mo and the samples grown below or above 900 °C. In addition, the overpotential of the films was approximately 249 mV at a geometric current density of 20 mA/cm^2, which was lower than that of the samples obtained at 700, 800, and 1,000 °C. Moreover, Tafel slopes originated from the polarization curves were obtained (Fig. 7(d)). The Tafel slope of the Mo_3B-900 (52 mV/dec) was a little higher than that of Pt foil (30 mV/dec) but distinctly lower than that of the samples grown at 700 °C (72 mV/dec), 800 °C (64 mV/dec), and 1,000 °C (94 mV/dec). The results indicate that the Mo_3B-900 has a higher catalytic rate and faster kinetics for HER. Figure 7(e) shows the electrochemical impedance spectroscopy (EIS) plots of the pure Mo foil and the samples obtained at different temperatures. It was expected that the Mo_3B-900 exhibited lower charge-transfer resistance (R_{ct}) value than the pure Mo foil and other samples on Mo foils, which further demonstrates a more rapid charge transport kinetics in Mo_3B-900. Figure 7(f) shows the comparison of the CV curves for the Mo_3B-900 at the first cycle and after 2,500 cycles. The almost identical cathodic current was observed, which implied that the Mo_3B-900 had a good catalytic stability. This work not only promotes the development of 2D metal borides in advanced HER electrocatalysis, but also points out a clear direction for 2D borophene in the field of energy conversion.

Although most of borophenes have been predicted to have higher catalytic activity than 2D metal borides, the experimental investigation of borophene in electrocatalysis has rarely been reported. Our group successfully prepared the borophene nanosheets on clean carbon cloth (CC) at 700 °C in H_2 gas by a typical CVD method [41] (Fig. 8(a)). As shown in Fig. 8(b), the borophene nanosheet with good crystallinity has lattice spacings of approximately 0.438 and 0.435 nm, which well correspond to those of the typical hydrogenated borophene (α'-2H-borophene) [39]. In addition, the α'-2H-borophene with zero bandgap exhibits metallic properties, which will facilitate charge transfer in the HER. The electrocatalytic HER performances of the borophene nanosheets were also evaluated in 0.5 M H_2SO_4 electrolyte using a standard three-electrode system. Figure 8(c) shows the LSV curves the samples synthesized at 600, 650, 700, 750, and 800 °C and a standard platinum (Pt) sheet as well as pure CC. By comparing the overpotential value of these catalysts at 10 mA/cm^2, it was found that the borophene nanosheets obtained at 700 °C (borophene-700) had an excellent HER performance and its overpotential was as low as 142 mV vs. reversible hydrogen electrode (RHE). Additionally, the samples synthesized at 600, 650, 750, and 800 °C respectively showed higher overpotential of 195, 159, 163, and 349 mV. Moreover, Tafel slopes of the samples were calculated to reflect their intrinsic catalytic activity (Fig. 8(d)). The Tafel slope of the borophene-700 was 69 mV/dec, which was much lower than that of the CC and the samples synthesized at other temperature conditions. The result indicates that the borophene-700 has high HER catalytic performance.

Furthermore, Fig. 8(e) shows the Nyquist diagrams of the CC and the samples synthesized at different growth temperatures. It was noted that the R_{ct} of the borophene-700

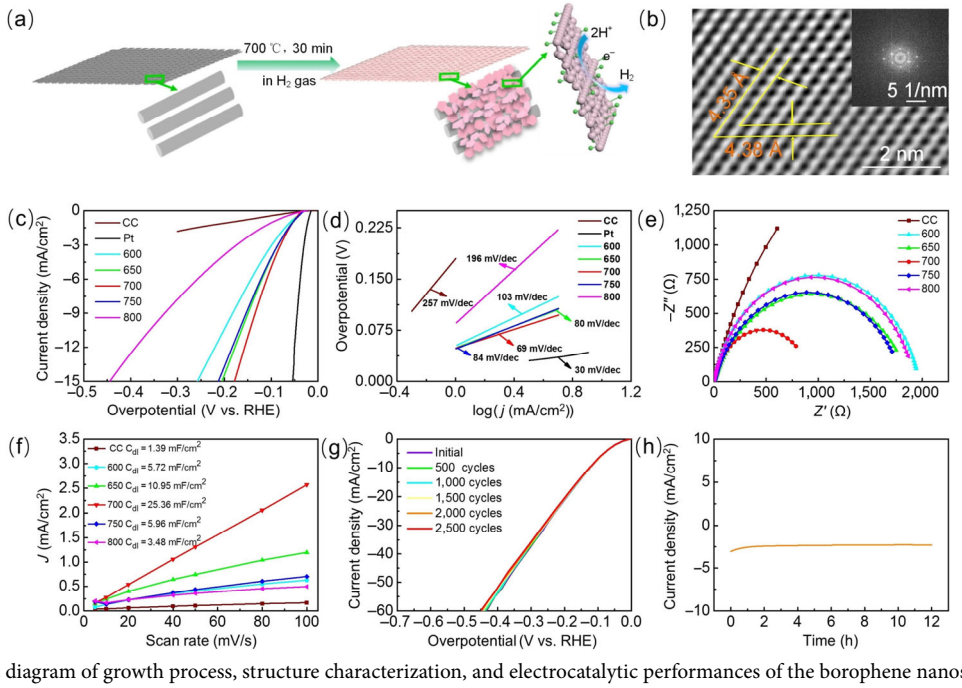

Figure 8 Schematic diagram of growth process, structure characterization, and electrocatalytic performances of the borophene nanosheets. (a) Schematic diagram of growth process of the borophene nanosheets. (b) HRTEM image of the borophene. (c) and (d) *IR*-corrected LSV curves (c) and the corresponding Tafel plots (d) of the samples grown at different temperatures. A standard Pt electrode and pure CC were selected as control experiments. (e) EIS Nyquist plots of the pure CC and the samples synthesized at different temperatures. (f) Plotting of capacitive current density against the scan rate for pure carbon cloth and the samples synthesized at different temperatures. (g) LSV curves of the borophene nanosheets synthesized at 700 °C at initial and after different cycles. (h) Long-term operation stability of the borophene nanosheets synthesized at 700 °C at a fixed overpotential of 0.1 V for 12 h. Reproduced with permission from Ref. [41], © American Chemical Society 2021.

was 1,349 Ω, which was the smallest value among the tested samples, further demonstrating that the borophene-700 had an outstanding catalytic activity. The double-layer capacitance (C_{dl}) of the samples was also calculated by the CV curve at different scanning rates. The C_{dl} of the borophene-700 was as high as 25.36 mF/cm^2, which mainly resulted from its excellent catalytic activity (Fig. 8(f)). The borophene-700 also exhibited a highly stable performance within typical accelerated degradation measurements for 2,500 CV cycles (Fig. 8(g)) and during a galvanostatic measurement at a fixed overpotential of 0.1 V for 12 h ((Fig. 8(h)). Concurrently, similar to the preparation strategy of monolayer γ_{28}-boron [27], our group has prepared triclinic boron nanosheets (BNS) on a clean tungsten (W) substrate by typical CVD technique. Differently, the mixed gases consisting of hydrogen (H_2; 10%) and argon (Ar; 90%) were selected as a protective and carried gas in the experiment. In addition, the boron nanosheets had shown excellent electrocatalytic HER activity, good cyclic stability, and long-term retention. The results pave a way for borophene in advanced energy conversion applications.

The anchoring of metal nanoparticles (NP) on the surface of 2D materials can be effective strategy to promote catalytic performance in HER [120, 121]. Borophene with large surface-area-to-volume ratio is able to be an ideal candidate to provide suitable anchored surface for the metal nanoparticles. In 2021, Chen et al. used a typical sonication-assisted liquid-phase exfoliation method to prepare high-yield, high-quality, and thin 2D BNS and then employed a rapid chemical reduction method to realize small-size rhodium nanoparticles anchored on BNS (Rh NP@BNS) [66]. The schematic diagram of the preparation process of the Rh NP@BNS is shown in Fig. 9(a). A typical AFM image shows that the thickness and lateral size of the BNS in the Rh NP@BNS are approximately 4 and 200 nm (Fig. 9(b)), respectively. In addition, the Rh NP with average diameter of about 3 nm are uniformly distributed within the boron nanosheets framework, which indicates the formation of the Rh NP@BNS. To investigate and evaluate the electrocatalytic activity of the Rh NP@BNS, a three-electrode system was used to test the HER performances in nitrogen-saturated 0.5 M H_2SO_4 (pH = 0.3) and 1.0 M KOH (pH = 14) as well as even the simulated seawater environment. Due to the similar testing procedure and performance analysis, electrocatalytic properties of the Rh NP@BNS in acidic solutions were emphatically analyzed in the review.

Figure 9(c) shows LSV curves of Rh NP@BNS in 0.5 M H_2SO_4. For comparison, bulk B, BNS, Rh NP, and commercial Pt/C were selected as control experiments. It was observed that the overpotential value at the current density of 10 mA/cm^2 could be identified at 66 mV for Rh NP@BNS, 163 mV for Rh NP, and 21 mV for commercial Pt/C (Fig. 9(d)). As expected, the Rh NP@BNS had higher catalyst activity than pristine BNS or Rh NP and could even rival the commercial Pt/C, which were originated from the strong interaction between the BNS and the Rh NP. Moreover, the consistent behaviors were also observed in the calculated Tafel plots in Fig. 9(e), where the Tafel slope was 56 mV/dec for Rh NP@BNS, 124 mV/dec for Rh NP, 159 mV for BNS, 219 mV/dec for bulk B, and 34 mV/dec for commercial Pt/C.

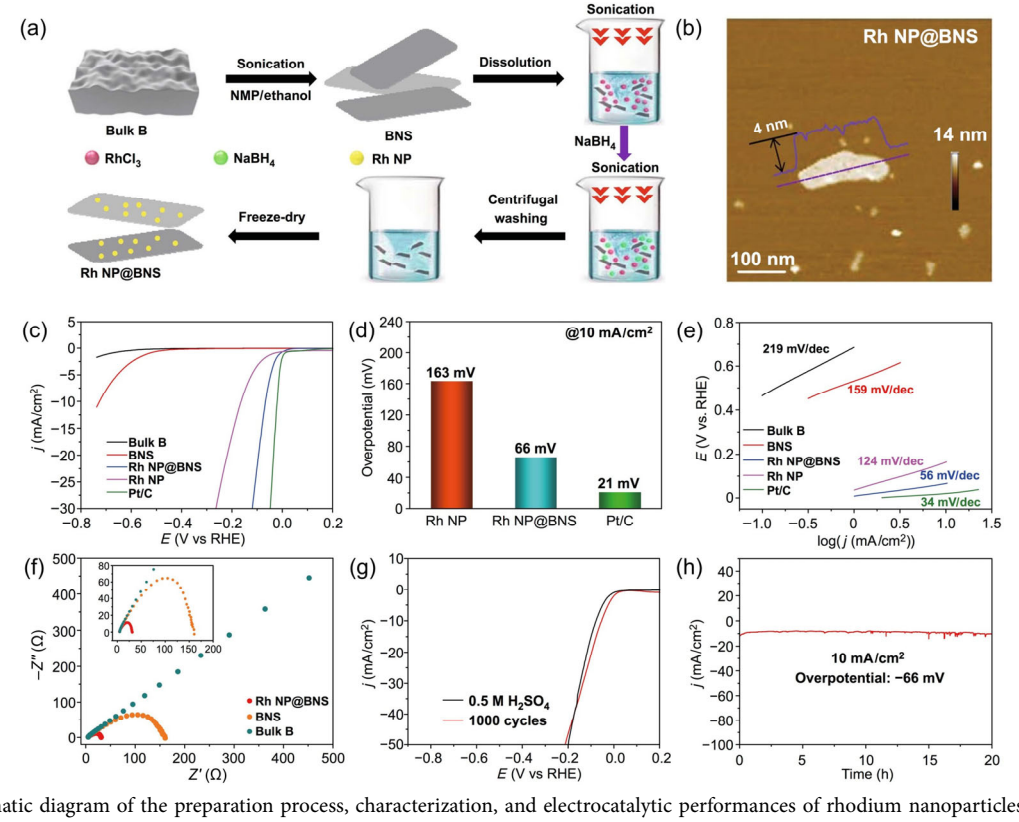

Figure 9 Schematic diagram of the preparation process, characterization, and electrocatalytic performances of rhodium nanoparticles anchored on 2D thin boron nanosheets (Rh NP@BNS). (a) Schematic diagram of the preparation process of the Rh NP@BNS. (b) AFM image of the Rh NP@BNS. (c) LSV curves of bulk B, BNS, Rh NP@BNS, Rh NP, and commercial Pt/C in 0.5 M H_2SO_4 electrolyte. (d) The overpotential of Rh NP, Rh NP@BNS and Pt/C at 10 mA/cm^2. (e) Tafel slopes calculated by LSV curves. (f) Nyquist plots of BNS, Rh NP@BNS, and bulk B. (g) LSV curves recorded before and after 1000 sweep cycles between 0.2 and −0.9 V (vs. RHE) in 0.5 M H_2SO_4 electrolyte. (h) Long-term operation stability of the Rh NP@BNS at a current density of 10 mA/cm^2 for 20 h. Reproduced with permission from Ref. [66], © Chen, K. et al. 2021.

The EIS was tested to reveal the charge transfer kinetics of the catalyst-coated electrodes during the HER process. Figure 9(f) shows the typical Nyquist plots of Rh NP@BNS, BNS, and bulk B. It could be found that the Rh NP@BNS had a lower charge-transfer resistance (31 Ω) than that of the BNS (160 Ω) and the bulk B (> 500 Ω), which suggested that the interaction between the BNS and the Rh NP could promote the electron transfer from the BNS to the Rh NP. Furthermore, good stability and high durability are regarded as an important criterion for the practical application of an electrocatalyst. To assess this good stability, the Rh NP@BNS catalyst was continuously cycled CV tests for 1,000 cycles (Fig. 9(g)). It was observed that the Rh NP@BNS after 1,000 cycles afforded almost similar curves as the initial state and had a negligible degradation of the cathodic current. Besides, long-term operational durability test results showed that the Rh NP@BNS catalyst could well maintain the current density for more than 20 h at 66 mV vs. RHE (Fig. 9(h)), suggesting that it had a high durability under electrolytic conditions. This work may provide new avenues or insights for the application of boron nanosheets or borophenes in the field of energy conversion.

Based on the theoretical predicts, it was suggested that the layered bulk magnesium diboride (MgB_2) powder was a potential boron source to synthesize borophene. In 2017, Nishino et al. prepared a novel HB nanosheets by simple exfoliation and ion-exchange between protons and Mg cations in MgB_2 [91]. Furthermore, the nanosheets showed a higher H_2-storage capacity than reported its bulk alloys and metal H_2-storage materials [92]. These works further promote the research of HB nanosheets for electrical information devices, photocatalysts, and electrochemical devices. Based on the preparation of HB nanosheets, Saad et al. used the HB nanosheets as a novel support for OER catalysts [67]. Figure 10(a) shows a schematic illustration of the preparation process of the electrocatalyst based on HB nanosheets. First, the HB nanosheets were prepared from MgB_2 by a simple chemical exfoliation method. Second, Ag ions can be reduced to Ag nanoparticles by the hydrogen (H) atoms on the surface of HB nanosheets. The other metal nanoparticles, such copper (Cu) nanoparticles and nickel (Ni) nanoparticles, can also be prepared by the similar process. Third, the Ag nanoparticles are beneficial to the formation of high-density Co_3O_4 nanoplates on the surface the Ag nanoparticles and HB nanosheets (Ag@B).

It was reported that the catalyst containing Ag nanoparticles could promote its electron transfer [122]. Besides, the interaction between the HB nanosheets and Co_3O_4 could stabilize Co_3O_4 nanoplates-Ag@B (Co_3O_4-Ag@B) structure and enhance the activity of the sites in Co_3O_4-Ag@B. Thus, the obtained Co_3O_4-Ag@B seems to be an excellent catalyst. To systematically evaluate the oxygen evolution activities of the Co_3O_4-Ag@B, a typical three-electrode system was used. To investigate the influence Ag^+ concentrations on electrocatalytic performance, two different Co_3O_4-Ag@B samples, named Co_3O_4-Ag@B^1 and Co_3O_4-Ag@B^2, were respectively prepared by using the Ag^+ concentrations of 7.0×10^{-2} and 3.5×10^{-2} mmol. Moreover, Co_3O_4-Ni nanoparticles-HB (Co_3O_4-Ni@B) and Co_3O_4-Cu nanoparticles-HB (Co_3O_4-Cu@B) were prepared to reveal the significance of the Ag nanoparticles in OER. Figure 10(b) shows hydrodynamic voltammograms of the Co_3O_4-Ag@B^1, Co_3O_4-Ag@B^2, Co_3O_4-Ni@B, Co_3O_4-Cu@B, and commercial IrO_2/C tested in a O_2-saturated 1.0 M KOH electrolyte. The corresponding overpotentials (η) obtained at the current density of 10 mA/cm^2 were 270, 283, 335, 360, and 310 mV, respectively. This proves that η increases with the decrease of the Ag^+ concentrations and Ag nanoparticles in catalyst can result in a lower η value than Ni and Cu nanoparticles. Tafel plots of the samples were calculated to understand the reaction mechanism. It could be found that Tafel slopes of the Co_3O_4-Ag@B^1, Co_3O_4-Ag@B^2, Co_3O_4-Ni@B, Co_3O_4-Cu@B, and IrO_2/C were respectively 62, 85, 96, 88, and

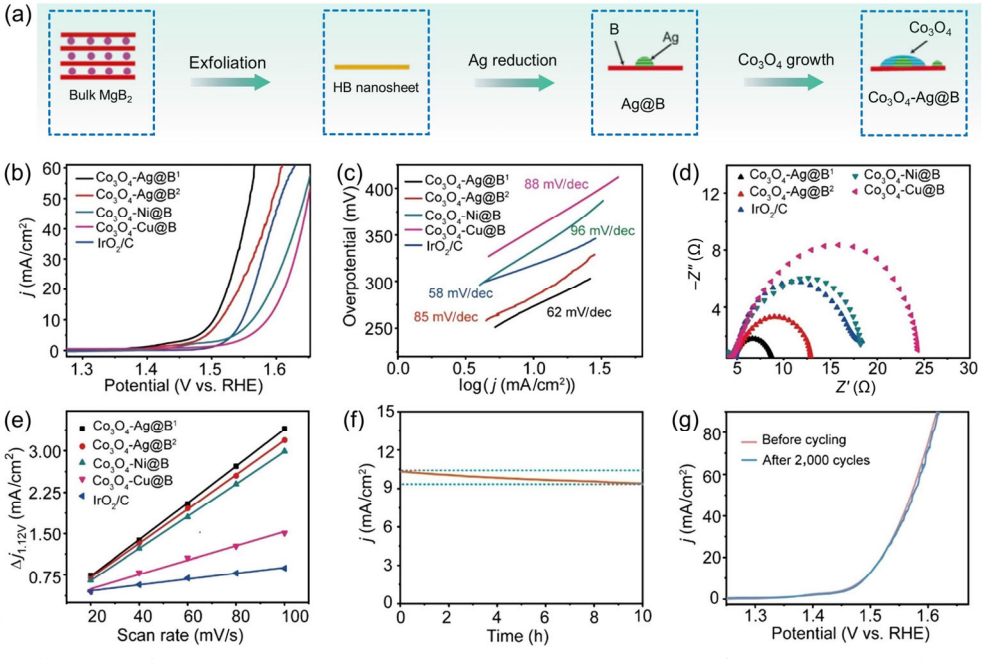

Figure 10 Schematic illustration of the preparation process and electrochemical characterization of Co_3O_4-Ag@B. (a) Schematic illustration of the preparation process of the Co_3O_4-Ag@B. (b) Hydrodynamic voltammograms of the samples: Co_3O_4-Ag@B^1, Co_3O_4-Ag@B^2, Co_3O_4-Ni@B, Co_3O_4-Cu@B, and IrO_2/C. (c) The corresponding Tafel plots of the samples. (d) Nyquist plots of the samples tested at 1.60 V potential vs RHE. (e) Plotting of capacitive current density against the scan rate for the samples. (f) Durability test of the Co_3O_4-Ag@B^1. (g) LSV curves of the Co_3O_4-Ag@B^1 were recorded before and after 2000 sweep cycles. Reproduced with permission from Ref. [67], © Elsevier B.V. 2021.

58 mV/dec (Fig. 10(c)). As expected, the Co_3O_4-Ag@B^1 has a higher catalyst activity than Co_3O_4-Ag@B^2, Co_3O_4-Ni@B, and Co_3O_4-Cu@B, and could even rival the commercial IrO_2/C. EIS was also tested to investigate the influence on the electrode kinetics. As shown in Fig. 10(d), the Co_3O_4-Ag@B^1 had a small charge transfer resistance of 5.6 Ω, which was lower than that of Co_3O_4-Ni@B (> 10 Ω) and Co_3O_4-Cu@B (> 10 Ω). The result indicates that Ag nanoparticles can provide a better electrical conductivity and faster charge transfer at the electrolyte and electrode interface than Ni and Cu nanoparticles in the catalysts. The C_{dl} of the catalysts was calculated by means of the CV curves tested at various scanning rates in the nonfaradaic current regions (Fig. 10(e)). The measured C_{dl} values were 16.6, 15.8, 14.6, 3.5, and 2.9 mF/cm^2 for Co_3O_4-Ag@B^1, Co_3O_4-Ag@B^2, Co_3O_4-Ni@B, Co_3O_4-Cu@B, and IrO_2/C, respectively. Figure 10(f) shows the stability test of the Co_3O_4-Ag@B^1 based on chronoamperometry. It was noted that there was no obvious degradation for the current density (10 mA/cm^2) after 10 h measurement. In addition, its stability was further verified by the polarization curves, which showed that the Co_3O_4-Ag@B^1 after 2,000 cycles afforded almost uniform curve shape as the initial state (Fig. 10(f)). The results also offer a novel direction for borophene in future energy conversion applications.

3.3 Borophene-based materials for energy harvesting

Because energy shortage and global warming have been threatening the development of human society, it is urgent to search and exploit new green energy resources. Natural water motions which ubiquitously exist on the earth are regarded as clean, green, and renewable energy resources. The nanoscience and nanotechnology have advanced by leaps and bounds, so some nanomaterials have been used to improve the conversion efficiency of the devices harvesting energy from water [123, 124]. It has been revealed that borophene with a special electronic structure will result in the rapid charge transfer between its surface and molecules or ions, which may be beneficial to energy harvesting devices [34].

Based on these, our group reported a novel borophene-based hydroelectric generator (HEG) which could harvest the electric energy from flowing water [40]. Figures 11(a) and 11(b) show the schematic diagram of the growth process of borophene glass. It could be experimentally realized by using sodium borohydride ($NaBH_4$) as a precursor and quartz as growth substrate in home-made CVD furnace with a low pressure and H_2-rich environment. A HRTEM image was used to reveal the structure of borophene. It can be observed that the crystal structure with the lattice spacing of 4.4 Å is well consistent with the previously reported α'-2H-borophene (Fig. 11(c)).

To establish a clean, efficient, and low-carbon energy system for meeting carbon neutralization, a novel and convenient HEG based on borophene glass, named BHEG, was fabricated. As shown in Fig. 11(d), according to the electrokinetic theory, the BHEG can continuously harvest electricity energy from flowing water. To verify the power generation capacity of the generator, the different incident angles and velocities of water flow on its surface were systematically investigated. A high induced voltage (−4.3 V) and current (−14 nA) were found at a fixed incident angle of 60° with a low flow velocity of 5 mL/s (Figs. 11(e) and 11(f)), which are superior to that of the other typical HEG based on nanomaterials. In addition, the generator could show an obvious ON/OFF effect during the water flow switching process.

To further investigate the relationship between the induced voltage and water flow velocity, different velocities at a fixed incident angle were performed on the surface of BHEG. It was observed that the induced voltage was proportional to the velocity, as shown in Fig. 11(g). Moreover, we also systematically revealed the influence incident angle on induced voltage at a fixed flow velocity of ~ 5 mL/s. When incident angle increased within 60°, the induced voltage value would increase along the negative potential direction (Fig. 11(h)). As the incident angle

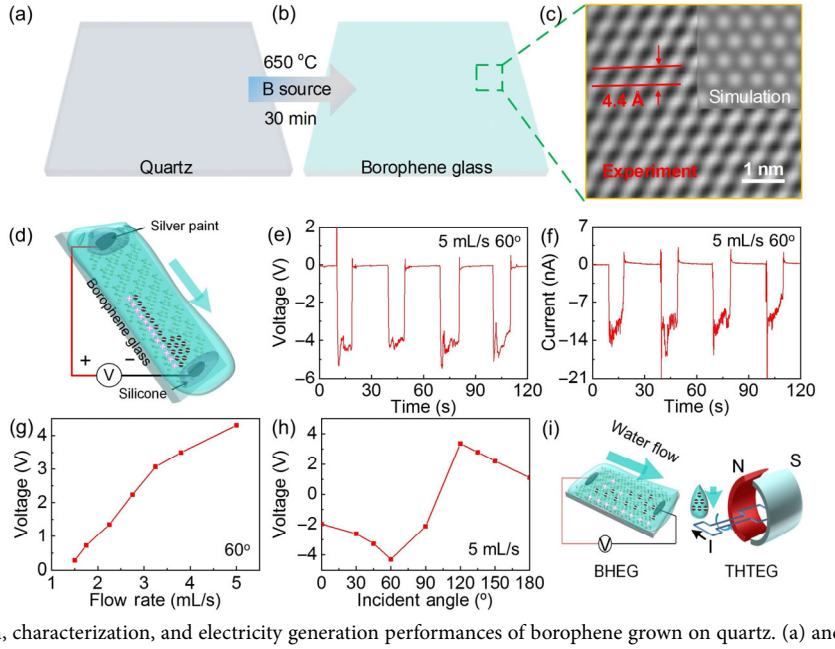

Figure 11 Growth diagram, characterization, and electricity generation performances of borophene grown on quartz. (a) and (b) Schematic diagram of growth process of borophene glass. (c) HRTEM image of borophene. (d) Schematic diagram of a fabricated borophene HEG (BHEG). (e) and (f) Induced (e) voltage and (f) current of BHEG with an incident angle of 60° and a water flow rate of 5 mL/s. (g) Relationship between the induced voltage and flow velocity. (h) Relationship between the induced voltage and the incident angle. (i) Working principles of the BHEG and traditional hydroelectric turbine generator (THTEG). Reproduced with permission from Ref. [40], © The Royal Society of Chemistry 2022.

increased to over 90°, the voltage transitioned to the positive potential direction (Fig. 11(h)). Subsequently, the induced voltage would drop after the incident angle reached over 120° (Fig. 11(h)). Because of the interaction between liquid flow and the borophene surface, the BHEG can effectively harvest energy in the absence of height difference (Fig. 11(i)). Contrarily, the traditional HEG must follow Faraday electromagnetic induction to produce electricity, which must be induced by the conversion of potential energy into kinetic energy (Fig. 11(i)). Compared with the traditional HEG, the novel BHEG with a facile and low-cost manufacturing process shows a great potential and good prospect for future green and clean energy.

In this section, we summarized the experimental progress of the borophene-based materials in the field of energy. Borophene not only shows great potential in supercapacitors, but also has good prospects in batteries. In addition, borophene has also been proven to be an excellent catalyst in electrocatalytic hydrogen production and electrocatalytic oxygen production. Besides, borophene has also been successfully applied to energy harvesting devices and exhibits excellent potential for energy harvesting from water. Borophene, as a promising 2D material, has great application prospects in the field of energy, so more experimental exploration is expected in the future.

4 Borophene-based materials for sensors

Electronic sensing devices, such as gas sensor, humidity sensor, pressure sensor, and photodetector, have attracted strong interest due to their great potential in health diagnosis, risk forecast, motions monitoring, and photonic signals detecting [125–128]. However, traditional sensing devices have several disadvantages: low sensitivity, slow response/recovery, and poor stability. To solve these challenges, a series of high-performance sensing devices based on novel 2D materials were fabricated [125–128]. Without exception, borophene has also been expected to be explored and used in the sensing field. Theoretically, it was predicted that atomic bonding in borophene could be formed between boron atoms and gas molecules and rapid charge transfer could be found between gas molecules and its surface [46–49]. Although the theoretical works have predicted that the borophene can be considered as a promising sensing material, the related experiments have slowly advanced for a long time because of the instability of its structure and the difficulty in transferring from the metal substrate. In recent years, as some stable borophene structures were synthesized, their sensing devices were successively reported.

4.1 Borophene-based materials for gas sensor

Ranjan et al. selected the boron nanosheets, which were prepared by sonochemical exfoliation method, as sensing layer and further fabricated an ammonia gas sensor on the sodium silicate substrate by a facile spin-coating method, showing high sensitivity and selectivity [56]. However, the corresponding sensing mechanism was not revealed systematically. In addition to the experimental synthesis of borophene, our group has also been devoted to fabricating the sensing devices based on borophene and achieved a series of innovative achievements in this field.

To investigate the gas-sensing properties of borophene, our group employed a facile and effective drop-coating method to fabricate a novel gas sensor based on hydrogenated borophene [68], which can realize efficient adsorption and desorption of nitrogen dioxide (NO_2) molecules and show an ultrasensitive response to NO_2 gas (Fig. 12(a)). To further evaluate the properties of the borophene NO_2 gas sensor, the related real-time response curve at the NO_2 concentration values from 0.2 to 100 ppm was obtained at room temperature (Fig. 12(b)). It could be found that the sensor showed high sensitivity and fast response to the different concentrations of NO_2, and the sensitivity would gradually increase with the increase of the concentrations. Additionally, the experimental limit of detection (LOD) was downed to 0.2 ppm, which was very suitable to its practical application in advanced chemical sensors. To further verify the possibility of its practical application, the exposure/recovery cycling tests at 50 ppm NO_2 were carried out at room temperature (Fig. 12(c)). It was observed that the sensitivity of borophene sensor had almost no noticeable degradation and the baseline did not drift. Moreover, compared with the borophene sensor in initial state, the sensitivity of the device hardly decreased after 30 days and still maintained a high level at 20 ppm NO_2 (Fig. 12(d)), which demonstrated that it had an excellent environmental stability at room temperature.

The underlying sensing mechanism has been systematically revealed by spin-polarized density functional theory (DFT) simulations. The results showed that a large number of electrons were accumulated in the vicinity of the NO_2 molecule and led to a significant charge redistribution, which caused the p-type doping of borophene. Thus, when the borophene sensor was exposed to the NO_2 gas environment, its conductivity would increase significantly. Contrarily, its conductivity would decrease with the decrease of the NO_2 concentration.

Because flexible and wearable properties also play an important role in its practical application, we have investigated the mechanical stability of the flexible polyethylene terephthalate (PET) substrate-based borophene gas sensor. Figure 12(f) shows a schematic diagram of the flexible borophene sensor in the bending state. We compared the sensor sensitivity in 2 ppm NO_2 gas between the initial state without bending (blue line) and the final state after 1,000 cycles of 90° bending (yellow line; Fig. 12(g)). It was noted that there was a slight fluctuation in sensitivity, which could be attributed to the effects of tension and compression. The results not only demonstrate the potential of borophene in practical applications, but also further promote borophene research in the field of sensors.

4.2 Borophene-based materials for humidity sensor

Because of their synergistic effects, 2D heterostructures have been proven to possess richer physicochemical properties than a single material [129, 130]. Stimulated by this characteristic, various heterostructures have been successively reported and already applied in high-performance electronic information devices [129, 130]. Borophene has been predicted to be an ideal candidate for the formation of heterostructures [95, 131], so the preparation and properties of its heterostructures are expected to be studied. To promote the rapid progress of borophene-based heterostructures, we have successfully prepared large-scale and high-quality borophene and graphene heterostructures by programmatically heating the mixture of the few-layered graphene (5 mg) and $NaBH_4$ powder (500 mg) [57]. Figure 13(a) shows a typical SEM image of the borophene–graphene heterostructures. It was found that the borophene–graphene heterostructures exhibited an obviously

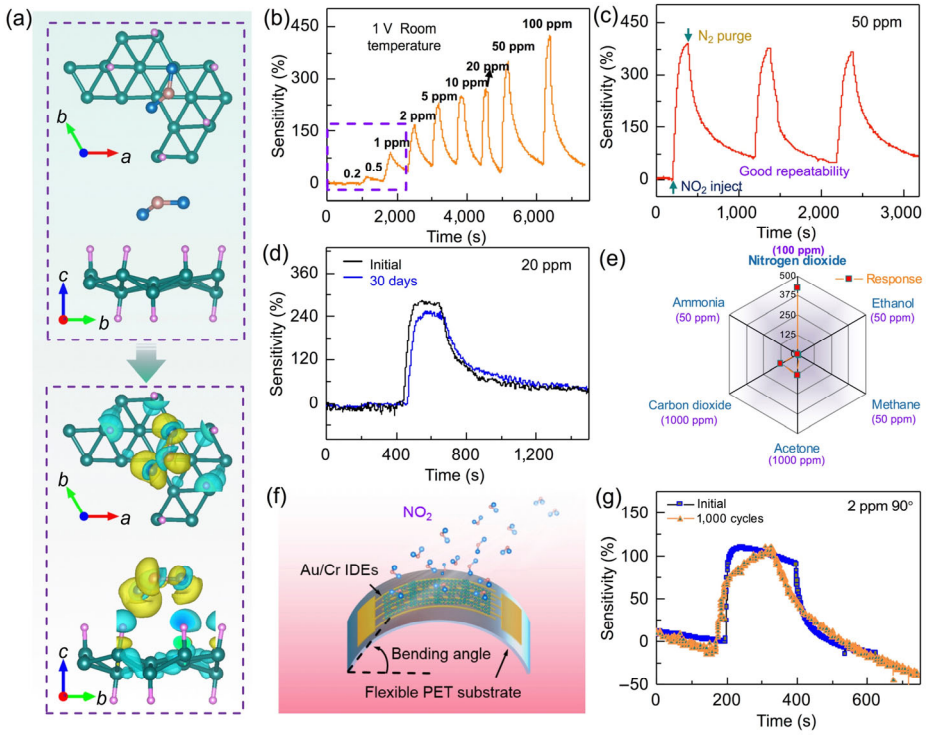

Figure 12 Gas-sensing properties of the borophene sensor at room temperature. (a) Schematic diagram of the interaction between the borophene and NO_2 molecules. (b) Response curves of the borophene sensor at different concentrations of NO_2. (c) Dynamic repeated stability of the sensor at 50 ppm NO_2. (d) Comparison of the sensor response to 20 ppm NO_2 before and after 30 days. (e) Sensitivity of the sensor at six typical gases with high concentration values. (f) Schematic diagram of the flexible PET substrate-based sensor in the bending state. (g) Comparison of the sensitivity of the sensor between the initial state without bending (blue line) and the final state after 1000 cycles of 90° bending (yellow line). Reproduced with permission from Ref. [68], © Tsinghua University Press and Springer-Verlag GmbH Germany, part of Springer Nature 2021.

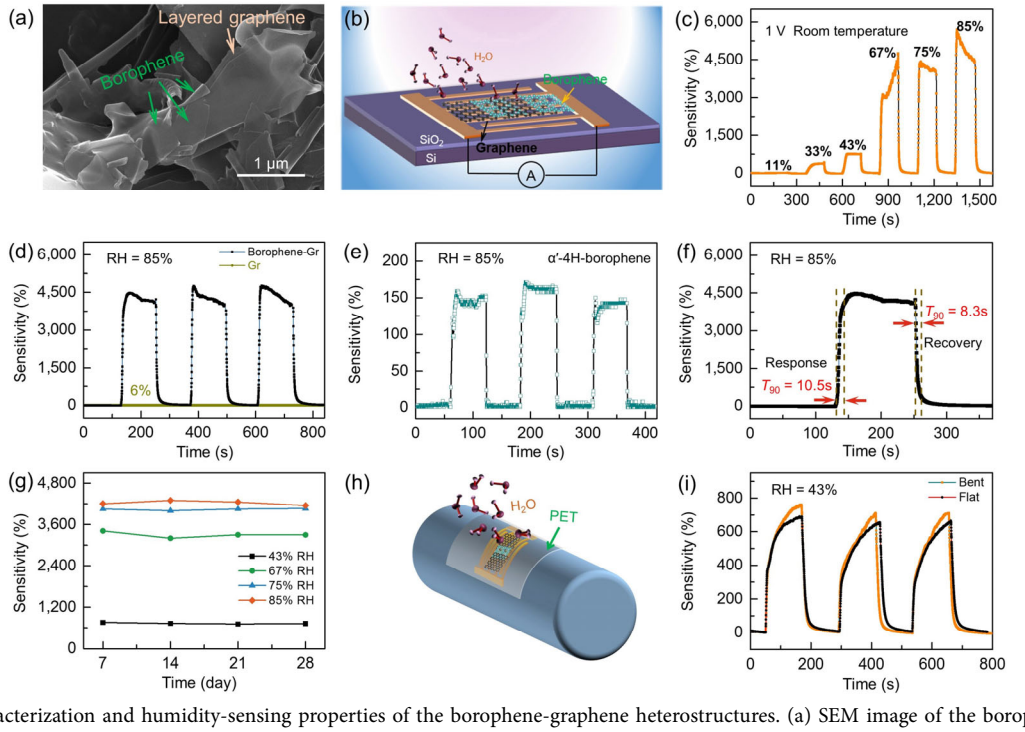

Figure 13 Characterization and humidity-sensing properties of the borophene-graphene heterostructures. (a) SEM image of the borophene–graphene heterostructures. (b) Schematic diagram of the borophene–graphene sensor. (c) Response curves of the borophene–graphene sensor at different switching RH values. (d) and (e) Dynamic repeated stability of the sensor based on borophene–graphene, graphene, and borophene at 85% RH. (f) Single response/recovery cycle curve of the borophene–graphene sensor at 85% RH. (g) Long-term environmental stability of the sensor at 43%, 67%, 75%, and 85% RH. (h) Schematic diagram of the flexible PET substrate-based sensor in the bending state. (i) Dynamic repeated stability of the flexible sensor in flat and bent states. Reproduced with permission from Ref. [57], © Tsinghua University Press and Springer-Verlag GmbH Germany, part of Springer Nature 2020.

stacked and hierarchical structure. In addition, large-scale and thin borophene sheets were observed on the outer surface of layered graphene, which proved the successful growth of borophene on the graphene surface and the formation of the borophene–graphene heterostructures.

Similar with the fabrication process of borophene NO_2 gas sensor, the resistive humidity sensor based on borophene–graphene heterostructures can also be obtained by the simple drop-coating method. Figure 13(b) displays the schematic diagram of the borophene–graphene sensor using SiO_2/Si as substrate. The humidity-sensing properties of the sensor were investigated by the typical switching relative humidity (RH) tests under different wet environments. Because the borophene–graphene sensor did not work when the RH value rose to 97%, the relative humidity range from 0% to 85% was used in subsequent experiments to explore the sensing performances. Figure 13(c) shows the response curves of the sensor at different wet environments of 0%, 11%, 33%, 43%, 67%, 75%, and 85% RH. When the relative humidity increased gradually, the sensitivity and current of the sensor would increase dramatically. Additionally, the highest sensitivity of the sensor was about 4,200% which was obtained at a high RH of 85% (Fig. 13(d)). According to the performance comparison of the sensors based on the heterostructure, borophene, and graphene, it was found that the borophene–graphene sensor showed the highest sensitivity among the sensors. The sensitivity of the borophene–graphene sensor was about 28 times that of the borophene sensor at 85% RH. Furthermore, the sensitivity of the borophene–graphene sensor was even up to 700 times that of the graphene sensor at 85% RH. The single response/recovery curves of the borophene–graphene humidity sensor were obtained at 85% RH, as shown in Fig. 13(f). It was noted that the sensors showed low response time (10.5 s) and recovery time (8.3 s). Long-term environmental stability of the sensor at 43%, 67%, 75%, and 85% RH was also systematically explored, as shown in Fig. 13(g). The result showed that the borophene–graphene sensor had excellent long-term environmental stability, which indicated the promising potential for practical application.

The sensing mechanism is similar to that of borophene NO_2 gas sensor. The adsorption of water molecules on the surface of borophene will result in the p-type doping of borophene. Besides, synergistic effects between borophene and graphene are another factor to promote the adsorption or desorption of water molecules. Thus, the synergistic effect could lead to a decrease in its resistivity when the borophene–graphene sensor was exposed to a wet environment. Conversely, the resistivity would increase with the increase of RH value.

Moreover, we replaced the rigid SiO_2/Si substrate with the flexible PET substrate to verify the mechanical stability of the borophene–graphene heterostructures. The schematic diagram of the PET-based borophene–graphene sensor in the bending state is shown in Fig. 13 (h). Figure 13(i) shows the response curves of the borophene–graphene heterostructures with and without applying bending strain at 43% RH. There was almost no significant difference for the test curves before and after bending, which exhibited that the heterostructures could be promising candidates for application in advanced wearable electronics.

In addition to the borophene–graphene heterostructures, we have successfully prepared the borophene–MoS_2 heterostructures by using *in-situ* van der Waals assembly method under facile ultrasonic irradiation. Figure 14(a) shows a typical low-resolution TEM image of the borophene–MoS_2 heterostructure. It could be found that the heterostructures were composed of ultrathin borophene sheets and layered MoS_2 sheets. In addition, the small-sized MoS_2 sheet closely contacted on the surface of a borophene sheet, which proved the formation of the borophene and MoS_2 heterostructure. Subsequently, a high-performance humidity sensor based on the borophene–MoS_2heterostructures was fabricated and the corresponding schematic diagram was shown in Fig. 14(b). Similar with borophene–graphene sensor, the humidity-sensing properties of the sensor were also explored by the typical switching relative humidity tests. Because the borophene–MoS_2 could work normally at 97% RH, the 0%, 11%, 33%, 43%, 67%, 75%, 85%, and 97% RH wet environments were selected (Fig. 14(c)). It was observed that the sensitivity and conductivity of the sensor would increase dramatically with the increase of relative humidity value. Additionally, the calculated highest sensitivity of the sensor obtained at a high RH of 97% was about 15,500%, which is the higher than that of the typical reported resistive sensors based on 2D materials or heterostructures: graphene (17%) [132], MoS_2 sheets (10,000%) [133], BP (521%) [134], borophene–graphene (4,200%) [57], and graphene–BP (43.4%) [135]. The sensor could maintain good cycle stability and repeatability under a three-cycle response in a wet environment of 97% RH (Fig. 14(d)). Figure 14(e) shows the single cycle response curves of the borophene–MoS_2 humidity sensor at 97% RH, which has a low response time (2.5 s) and recovery time (3.1 s). Moreover, we also systematically investigated long-term environmental stability of the borophene–MoS_2 sensor at 43%, 67%, 75%, 85%, and 97% RH, as shown in Fig. 14(f). The results indicated that the sensor had a good long-term environmental stability, which would be beneficial for long-life electronic sensor systems.

The excellent sensing performances of the borophene–MoS_2 sensor endow it broad application prospects for human health monitoring (Fig. 14(g)) and non-contacted smart systems (Figs. 14(h) and 14(i)). To better verify the recognition ability of the sensor for respiratory frequency, different breathing rates generated by different scenarios were explored. Figure 14(g) shows the response results at low respiration frequency with resting and high respiration frequency after exercise. It was found that the change of current could completely correspond to the process of breathing and the respiration frequency could be easily obtained by the curves. Thus, the results not only further demonstrate the reversibility and good stability of the sensor, but also expand the application of the sensor in the field of health monitoring. Besides, we also fabricated a typical non-contact smart system which was mainly composed of a borophene–MoS_2 sensor, a white LED light, and a protective resistor (Fig. 14(h)). When a fingertip was close to the sensing layer of the sensor, the inducing current of the LED would increase, which could result in the LED turning on (ON state, Figs. 14(h) and 14(i)). When the fingertip was removed from the sensing layer, the current would decrease which could give rise to turning off the LED (OFF state, Figs. 14(h) and 14(i)).

4.3 Borophene-based materials for pressure sensor

Wearable or skin-like pressure sensors, which show good response to small force fluctuations, have received extensive attention in robotic technologies, health monitoring and diagnose systems, human–machine interfaces (HMIs), and even artificial intelligence devices [127]. Although some typical

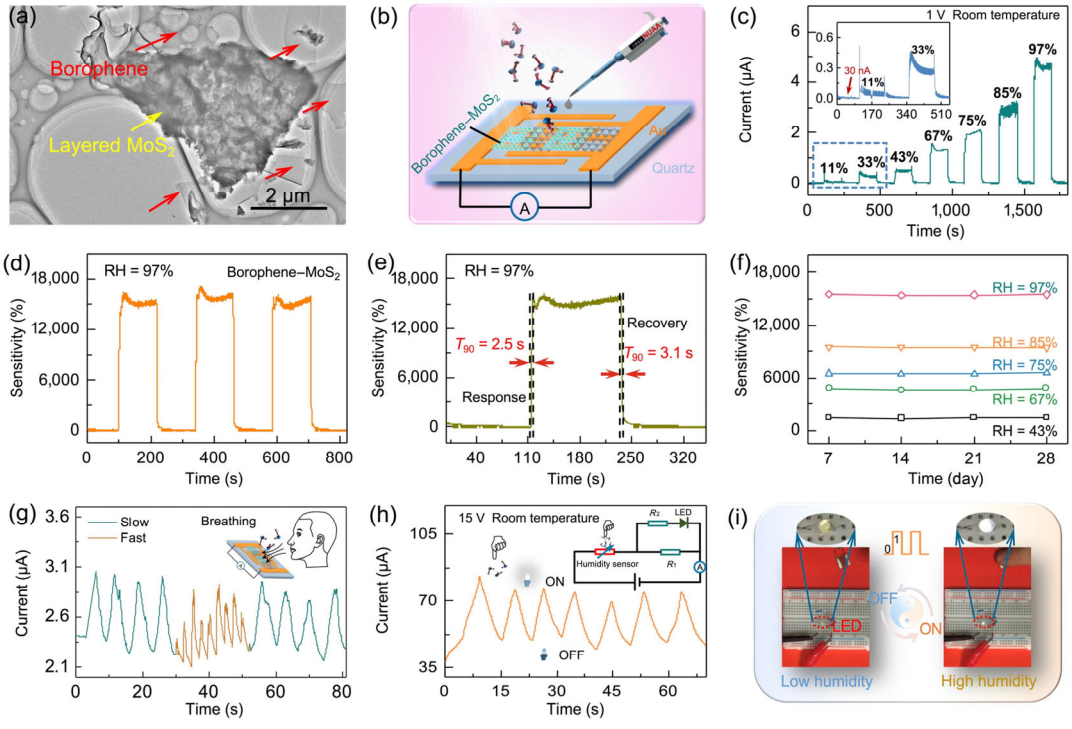

Figure 14 Characterization, humidity-sensing properties, and multifunctional applications of the borophene–MoS_2 heterostructures. (a) TEM image of the borophene–MoS_2 heterostructures. (b) Schematic diagram of the borophene–MoS_2 sensor. (c) Real-time response curves of the sensor at different switching RH values. (d) Dynamic repeated stability of the borophene–MoS_2 sensor at 97% RH. (e) Response and recovery cycle curve of the sensor at 97% RH. (f) Long-term environmental stability of the sensor at 43%, 67%, 75%, 85%, and 97% RH. (g) Response to different respiratory rates. (h) Current response and circuit diagram of the non-contact switch sensing system. (i) Photographs of the noncontact switch sensing system. Reproduced with permission from Ref. [58], © The Royal Society of Chemistry 2021.

nanomaterials with good conductivity have been considered or used in pressure sensors, several drawbacks are inevitable: narrow pressure detection range, poor integration with semiconductor process, and high-power consumption with low open circuit resistance. To solve the problems and further improve the sensing performances, a novel pressure sensor based on semiconducting hydrogenated borophene has been fabricated by a facile, eco-friendly, and low-cost approach [69].

As shown in Fig. 15(a), the novel borophene pressure sensors could be assembled by stacking the sensing layer which was composed of borophene and tissue paper onto the cutted printed paper substrate with Cr/Au interdigitated electrodes (IDEs). Figure 15(b) shows the current–voltage (I–V) characteristics of the borophene pressure sensor under various applied static pressures. When a static pressure in the range of 0 to 120 kPa was sequentially applied to the sensor, the current would change significantly and increase with increasing the pressure. According to dynamic pressure response tests, the piezoresistive sensitivity (S) of the borophene pressure sensor was calculated, which could be expressed as $S = \delta(\Delta I/I_0)/\delta P$, where ΔI, I_0, and P represent the current changing, the initial current, and the applied dynamic pressure on the sensor, respectively. It was observed that the sensitivity of the borophene pressure sensor was close to 2.16 kPa^{-1} when the loading pressure was < 1.2 kPa (Fig. 15(c)). Subsequently, when the applied pressures increased from 1.2 to 25 kPa, the sensitivity would decrease to about 0.13 kPa^{-1} (Fig. 15(c)). Moreover, when applied pressure was more than 20 kPa, the bulk matrix deformation became the dominant factor to influence the sensitivity. So, it was down to approximately 0.07 kPa^{-1} (Fig. 15(c)). The borophene sensor displayed excellent reproducibility, long-term durability, and high stability under a pressure impact of ~ 10 kPa during 1,000 dynamic loading and unloading cycles (Fig. 15(d)). The pressure sensing mechanism is similar to that of the other reported paper-based pressure sensor, which is mainly resulted from the change of contact resistance between the borophene/tissue paper and the IDEs under external pressure.

Excitedly, the flexible borophene sensor had shown its multifunctional applications in human health monitoring and diagnosis (Fig. 15(e)), recognition of real-time phonation (Fig. 15(f)), human motions detection (Fig. 15(g)), soft skin for sensing touch (Fig. 15(h)) and HMI (Fig. 15(i)). Figure 15(e) shows that the borophene sensor could accurately record and distinguish the real-time wrist pulse signals of 26-year-old healthy volunteer. It was noted that there were ~ 72 peaks within 1 min, which corresponded to 72 heart rate beats per minute. Moreover, four obvious wave characteristics of starting point (S), percussion (P), trial (T), and dicrotic (D) were found, which could be regarded as important information to analyze the heart diseases.

Real-time pronunciation recognition test was also explored by attaching a borophene skin sensor on the throat of the volunteer. When the speaker repeatedly said the word of "borophene" for three times, the current–time curves demonstrated the almost same peak shapes (Fig. 15(f)). Thereby, the skin sensor had great application prospects in a speech recognition system by sensing the movement or vibration of muscles when a person pronounced.

Further, we also investigated the potentials of the skin sensor for real-time human motion monitoring. Figure 15(g)

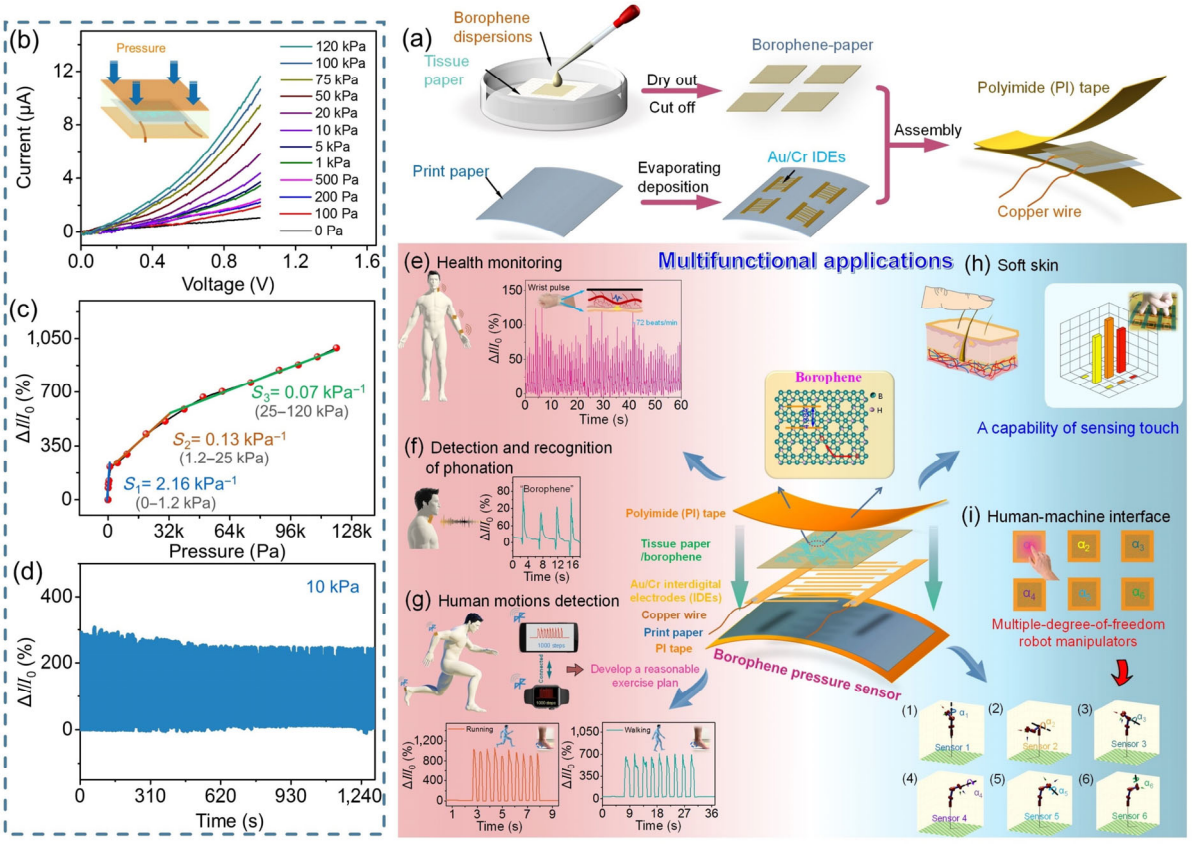

Figure 15 Fabrication process, electromechanical performances, and multifunctional applications of the borophene pressure sensor. (a) Schematic diagram of fabrication process of the pressure sensor based on borophene and tissue paper. (b) Current–voltage (I–V) characteristics of the fabricated borophene sensor under various applied pressures. (c) Piezoresistive sensitivity of the borophene sensor. (d) Performance of the borophene sensor under repetitive pressure loads of ~ 10 kPa for 1000 cycles. (e)–(i) Multifunctional applications of the borophene pressure sensor: (e) health monitoring, (f) detection and recognition of phonation, (g) human motions detection, (h) soft skin, and (i) human–machine interface. Reproduced with permission from Ref. [69], © Elsevier Ltd. 2022.

shows the response curves of the borophene sensor during running and walking. The change of $\Delta I/I_0$ values could be attributed to the compression between the leg muscles and the soles of the shoes. The $\Delta I/I_0$ curves generated by running and walking showed a good stability and excellent repeatability. Additionally, the sensor also showed an ability to accurately detect and distinguish the different motion rates.

A tactile simulation system which was composed of a 3 × 3 pixel borophene sensor array and the related circuit was fabricated. When three fingertips touched on the surface of the sensor in the array, three histograms would immediately occur on the monitor (Fig. 15(h)). On the contrary, the histograms would quickly disappear as the fingertips moved away. These can correspond to the process of the touch or mechanical stimulation on human skin. Thus, the results indicate that the borophene-based electronic skin (e-skin) is able to realize the perception of mechanical stimulation like human skin, which will provide a simple and effective manufacturing method and a novel nanomaterial system for the field of intelligent e-skin.

The multiple-degree-of-freedom control of the robotic arm is a key factor for its practical application in HMI. A virtual control system which consisted of an array with six borophene sensors, virtual robotic arm model, and data acquisition module was constructed to realize the simulation of robotic arm motions (Fig. 15(i)). The joints of the virtual robotic arm could be manipulated by the borophene pressure sensor array. When a pressure was applied on the surface of a sensor in the array, it would cause an obvious rotation of the joint in the virtual robotic arm. In addition, each sensor in the array could precisely realize a specific form of rotation of the robotic arm (Fig. 15(i)). Impressively, the control system had also an ability to achieve the coupling and the linkage of the joint, which was beneficial to its practical application in HMI field. Above all, the results pave the way of borophene in the field of pressure sensor and also expand the application of borophene in the field of sensor.

4.4 Borophene-based materials for photodetector

In addition to the exploration of the borophene-based materials in chemical and pressure sensors, it has been systematically investigated in the field of photodetector. Ma et al. reported the optoelectronic performances of the exfoliated boron sheets by fabricating their photoelectrochemical-type (PEC-type) and FET-type photodetectors [70]. The results indicated that the PEC-type device not only showed a self-powered capability, but also had a high photoresponse to ultraviolet (UV) light (2.9–91.7 μA/W). Besides, the FET-type photodetector exhibited a tunable high photoresponsivity (174–281.3 μA/W) under the illumination of excited light with the wavelength of 405 nm. Although the both types of photodetectors showed low responsivity at the level of μA/W, the work could pave the way for the practical applications of the novel boron sheets in optoelectronic devices.

To further advance borophene-based applications in the field of photoelectric detection, our group employed CVD method to grow large area continuous α'-2H-borophene film and then transferred it onto n-type silicon substrate to fabricate Schottky junction (borophene-Si) photodetector [39]. The schematic view and the corresponding photograph of the device structure are shown in Fig. 16(a). The device had a high rectification ratio of 10^2 measured at ±5 V in the dark (Fig. 16(b)). In addition, the photocurrent of the device was also measured with the different power intensities in the range of 3.63–31.3 mW/cm^2 under the irradiation of 625 nm LED light (Fig. 16(c)). It could be found that the photocurrent density was proportional to light illumination intensity at a reversed bias of 4 V (Fig. 16(d)). Moreover, the measured responsivity (R) was over 1.04 A/W under a light power intensity of 5.73 mW/cm^2 at 4 V.

Figure 16(e) shows the multi-cycle temporal response curves obtained under tunable light illumination from 3.63 to 31.3 mW/cm^2 at 4 V. The corresponding photocurrent of the device could retain from 0.15 to 0.80 mA during the cycling tests, which proved the good stability of the device (Fig. 16(e)). Besides, the single-cycle temporal response curves measured under the illumination power of 5.73 mW/cm^2 showed that the device had a low response time of 0.4 s and recovery time of 0.6 s (Fig. 16(e)). Ignited by the breakthrough, a novel borophene–ZnO ultraviolet detector was also fabricated by our group [59]. Similarly, the ultraviolet detector showed a high photoresponsivity (0.102 A/W), a high specific detectivity (1.43×10^9 Jones) at a reversed bias of −5 V, and fast photoresponse speed (~ 3 s). Thus, these excellent optoelectronic performances endow borophene and its heterostructures unlimited possibilities in advanced and high-performance optoelectronic devices.

In this section, we summarized the experimental progress of the borophene-based materials in the field of sensors. Borophene not only exhibits sensitive response to toxic gases, but also can be successfully used as a sensing layer to achieve a small pressure response. In addition, its heterostructures, such as borophene–graphene and borophene–MoS_2, have excellent humidity-sensitive properties and also show good application prospects in human health monitoring and non-contact sensing. Besides, borophene can be also a promising material for fabricating high performance photodetectors. Experimental study of borophene in the sensing field is only in its infancy, more efforts should be made in subsequent experimental exploration.

5 Borophene-based materials for information storage

The rapid progress of modern electronic technology has promoted the in-depth exploration of high-performance data storage devices [136, 137]. Resistor-type memory devices, which are composed of an active material sandwiched between two different-type electrodes, have been considered because of their structural simplicity and electrical bistability [136]. The typical three-dimensional stacked structure endows it possible to have high capacity data storage. It has been proven that some novel low-dimensional nanomaterials, including MoS_2, BP quantum dots, and carbon nanotubes, can hybrid with polymers to form attractive active layer for the fabrication of next-generation resistive memory devices [136]. However, high switching voltage and poor long-term stability limit them for the real information storage in electronics. Therefore, more emerging nanomaterials are being systematically investigated to compensate for the above limitations. Borophene, as a rising star in nanomaterials, has also been explored by fabricating its non-volatile resistive memory devices in recent years.

To promote the stability of borophene and further advance its application in information storage devices, our group first developed an effective *in-situ* three-step thermal decomposition of sodium borohydride to synthesize large-size semiconducting hydrogenated borophene (α'-4H-borophene) [37]. The corresponding schematic diagram of preparation process of the hydrogenated borophene is illustrated in Fig. 17(a). As shown in Fig. 17(b), the borophene showed good crystallinity with an obvious hexagonal lattice, which is in good agreement with the structure of the predicted α'-4H-borophene. Furthermore, it was demonstrated that the borophene not

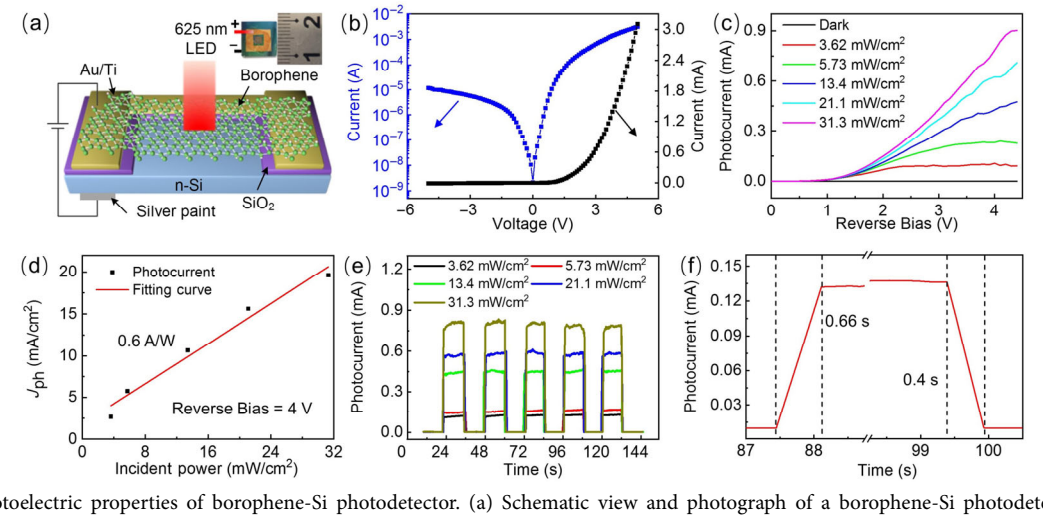

Figure 16 Photoelectric properties of borophene-Si photodetector. (a) Schematic view and photograph of a borophene-Si photodetector under the irradiation of LED light of 625 nm. (b) Current–voltage (I–V) characteristics of the borophene-Si photodetector in the darkness. (c) Dark and illuminated current versus applied reversed biases which depends on the incident power under 625 nm LED illumination. (d) Photocurrent as a function of incident power at a reverse bias of 4 V. (e) Temporal response of the borophene-Si photodetector measured under different light intensities at 4 V. (f) The single temporal response curves under the incident power of 5.73 mW/cm^2. Reproduced with permission from Ref. [39], © American Chemical Society 2021.

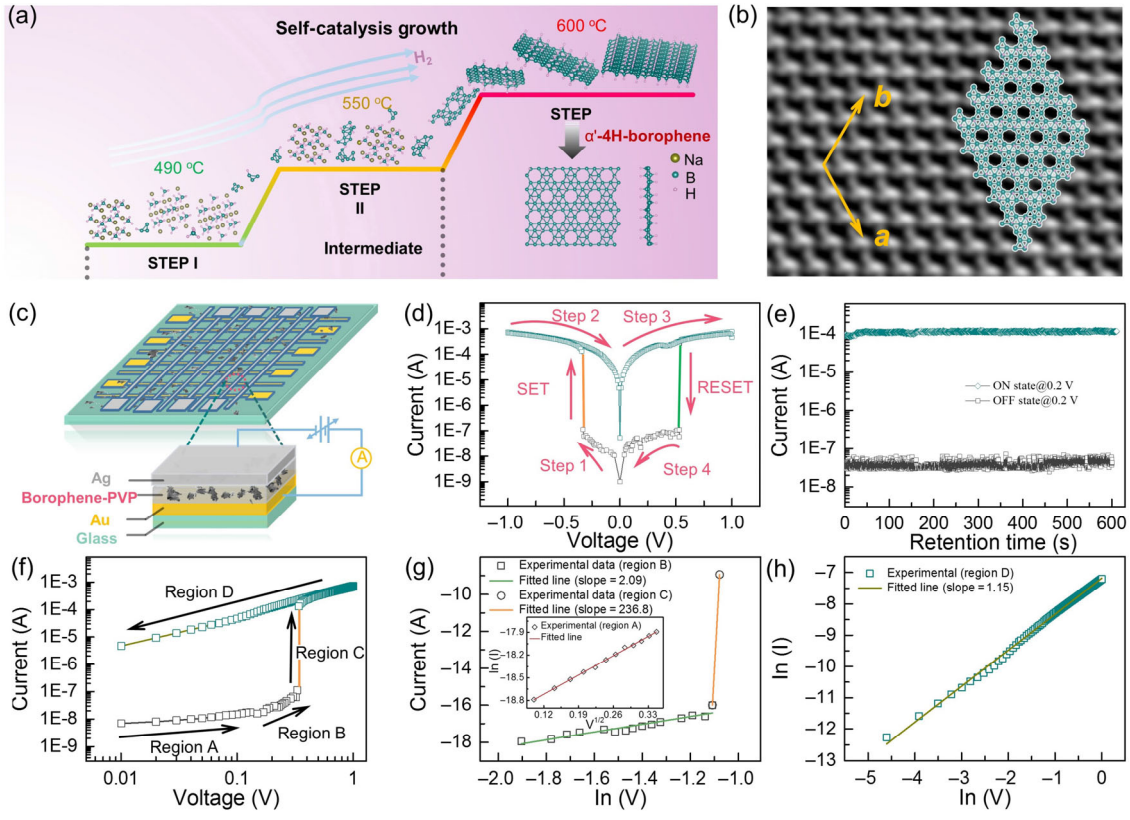

Figure 17 Growth process, characterization, and memristive performances of hydrogenated borophene. (a) Schematic diagram of growth process of the hydrogenated borophene. (b) High-resolution image and crystal structrue of the borophene. (c) Schematic illustration of the borophene-based memory device. (d) Current–voltage (*I*–*V*) curves of the borophene memory. (e) Long-term retention test of the memory at ON and OFF states at 0.2 V. (f) *I*–*V* characteristics of the memory during Steps 1 and 2 processes. (g) and (h) Linear fitting curves based on the experimental data at (g) OFF and (h) ON states. Reproduced with permission from Ref. [37], © Wiley-VCH Verlag GmbH & Co. KGaA, Weinheim 2020.

only had excellent sensing, catalysis, and energy storage properties in the above-mentioned works, but also exhibited competitive information storage properties. To systematically evaluate its information storage properties, a novel borophene-based memory device was fabricated by using the α'-4H-borophene sheets as the active layers and the poly(vinylpyrrolidone) (PVP) as the insulating layers. The schematic illustration of the borophene-based memory device is shown in Fig. 17(c).

A typical voltage scanning test showed that the borophene memory device exhibited a distinct bistable behavior (Fig. 17(d)). When the applied voltage was swept from 0 to −1 V during Step 1 process, the device would transit from high-resistance state (HRS; OFF state) to the low-resistance state (LRS; ON state) at a low set voltage of around 0.33 V, which could be regarded as data writing of a digital memory. Then, the device stably maintained at ON state within the sweeping voltage from −1 to 1 V during the Steps 2 and 3. Another transition occurred during the sweeping voltage from +1 to 0 V (Step 4), which could correspond to the data erasing of a digital memory. Moreover, the stability of the device was also investigated by typical maintain-ability measurement, as shown in Fig. 17(e). It was found that the current had no significant degradation or upgradation during the retention time of 10 min, which demonstrated its good stability. Additionally, an ON/OFF current ratio measured at 0.2 V was found to be as high as 3,000.

The conduction mechanism of the borophene/PVP memory device had also been revealed by the *I*–*V* characteristics, as shown in (Fig. 17(f)). The relationship between voltage and current could be linearly fitted by the plot of ln(*I*) vs $V^{1/2}$ in the voltage range from 0 to −0.12 V (region A; Fig. 17(g)), which could correspond to the typical thermionic emission [138, 139]. When the voltage increased from −0.12 to −0.35 V (region B), there was a nonlinear relationship between voltage and current, which could be fitted by the plot of *I* vs V^2 (Fig. 17(g)). The conductive behavior was well consistent with the typical space charge limited conduction (SCLC) model. After the voltage continued to increase and exceeded −0.35 V (region C), injected carriers in the borophene would increase exponentially (Fig. 17(g)). The results would give rise to a higher electron concentration, which made the device have lower resistance and then transit to ON state. When the device maintained at the ON state, it exhibited a typical Ohmic behavior (slope ~ 1.15) in region D (Fig. 17(h)), which could be attributed to the formation of filament paths after the SET process. On the contrary, when the reverse bias was applied, the trapped charges were easy to be neutralized, which caused the device return to the OFF state. The results indicate that the device can successfully achieve the re-written and re-erased process, which suggests the promising potential of the borophene in high-performance electronic information storage devices.

Stimulated by the successful fabrication of the borophene memory device, the borophene-based heterostructures memory devices were successively reported. In 2021, a novel borophene-based core–shell structure was prepared by heating a homogeneous mixture of Fe_3O_4 nanoparticles and $NaBH_4$ powder in multiple steps [71]. Then, similar to the construction of above-mentioned borophene-based memory,

a high-performance and stable memory based on the borophene–Fe_3O_4 core–shell nanoparticles was fabricated. The memory showed a low reset voltage of about 0.19 V and a high ON/OFF current ratio of around 8.23×10^5.

Recently, we also successfully prepared borophene–ZnO heterostructures by dispersing the borophene sheets in ZnO QDs dispersions via ultrasonication process for 2 h, and fabricated the corresponding broadband photonic nonvolatile memory by the same manufacturing process as the borophene memory device (Fig. 18(a)) [60]. The basic nonvolatile memristive properties were systematically investigated, exhibiting high ON/OFF ratio, low SET/RESET voltage, and long-term cycling stability. Besides, because the fast exciton splitting rate and enhanced photon trapping behavior were found in the borophene–ZnO heterostructure, it was necessary to explore the optoelectronic coupling properties of its memory. Figure 18(b) shows *I*–*V* curves of the borophene–ZnO memory under the illumination of 365, 520, 600, and 850 nm LED light with a same illumination intensity of 300 μW/cm^2. Compared to the device in dark, there was a significant drop in the SET or RESET operating voltage under the illumination of different wavelengths LED light. Additionally, the voltage would decrease as the wavelength became shorter, which was caused by the separation of photoexcited electron holes from borophene–ZnO heterojunction, which will promote the formation of conductive filament paths and then accelerates SET process. The decrease of the RESET voltage could be attributed to the Joule heating effect originated from large current flow, which would accelerate the disappearance of the conductive filament paths.

Furthermore, the SET process of the device was tested at different irradiation wavelengths 365 nm (UV), 520 nm (green), 600 nm (red), and 850 nm (near infrared ray (NIR)) with various light illumination intensities, respectively (Figs. 18(c)–18(f)). It was observed that there was an obvious decrease for the SET voltage when the light illumination intensity decreased under any wavelength of light irradiation (Figs. 18(c)–18(f)). Additionally, the transition voltage would increase from 1.9 to 3.2 V with the increased wavelengths from 365 to 850 nm (Figs. 18(c)–18(f)). The phenomenon can result from the influence of photovoltaic and photoelectric effects on the formation and disappearance of oxygen vacancy (O_V) filament paths. Therefore, the results not only provide a promising novel material system for next-generation information storage devices, but also pave the way for borophene-based memory toward high-speed, low-cost, and multilevel broadband photonic resistive random access memory (RRAM).

Besides, our group has prepared uniform and high quality borophene quantum dots and fabricated their rewriteable nonvolatile memory device (Figs. 18(g)–18(i)) [140]. Similarly, the typical *I*–*V* characteristics curves were tested to evaluate the performances of the device (Fig. 18(h)). It was demonstrated that the device displayed an obvious electrical bistability and a low set voltage of 0.5 V (Fig. 18(h)). There was no significant fluctuation in long-term retention curves (Fig. 18(i)). These

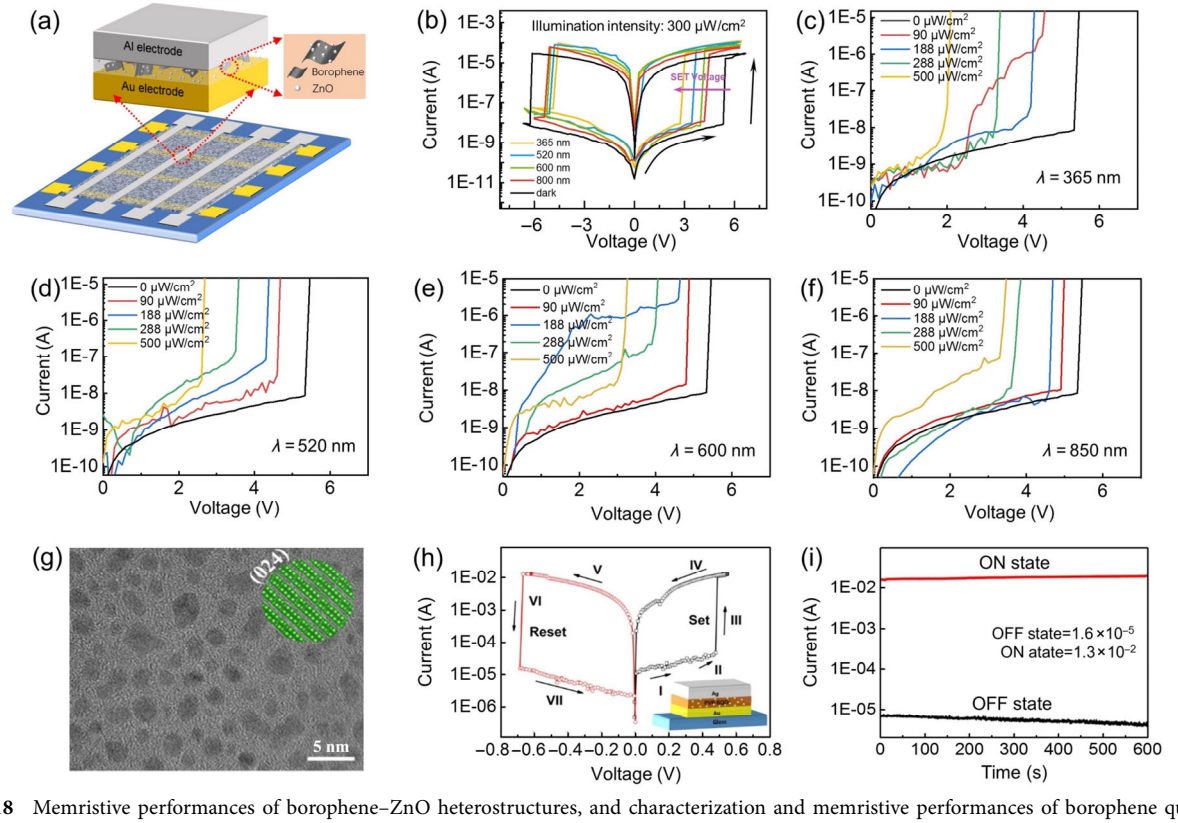

Figure 18 Memristive performances of borophene–ZnO heterostructures, and characterization and memristive performances of borophene quantum dots. (a) Schematic illustration of the borophene–ZnO memory device. (b) Current–voltage (*I*–*V*) curves of borophene–ZnO memory under the illumination of 365, 520, 600, and 850 nm LED light with a same illumination intensity of 300 μW/cm^2. (c)–(f) *I*–*V* curves of the memory under different irradiance intensities (0 to 500 μW/cm^2) at various wavelengths: (c) 365, (d) 520, (e) 600, and (f) 850 nm. (a)–(f) Reproduced with permission from Ref. [60], © Tsinghua University Press 2022. (g) HRTEM image and crystal structrue of the borophene quantum dots. (h) *I*–*V* curves and schematic diagram of the memory based on borophene quantum dots. (i) Long-term retention test of the memory in ON and OFF states at 0.1 V. (g)–(i) Reproduced with permission from Ref. [140], © American Chemical Society 2020.

revealed that the borophene quantum dots had a good prospect in practical memory devices. Recently, borophene nanosheets which were synthesized by a facile probe ultrasonic approach were selected as an active layer in memory devices, which also showed a rewriteable nonvolatile memory behavior and good stability. Although a series of experimental explorations of borophene and its heterostructures in the field of information storage have been carried out, the field is still in its infancy and more efforts are needed to achieve high-density data storage towards its practical applications.

In this section, we introduced the experimental research of borophene and its heterostructures in the field of information storage. Borophene can be regarded as an excellent active material for fabricating memory devices, which can show ultra-low operating voltage, high switching ON/OFF ratio, and long-term stability. Stimulated by the experimental research, borophene–ZnO heterostructures have also been considered for use in memory devices. The borophene–ZnO memory not only maintains excellent memristive performances, but also shows a broad light response. Although borophene has shown great application prospects in the field of information storage, there are still few relevant experimental reports. Therefore, more efforts need to be made to promote the development of the field.

6 Summary and future outlook

In summary, the review comprehensively summarized recent experimental advances of borophene-based materials in the fields of energy, sensors, and information storage. Borophene-based materials, as a promising electrode material, have been successfully applied in high-performance supercapacitors and rechargeable novel batteries. In addition, borophene-based materials with a large number of active sites have been demonstrated to be a highly efficient catalyst for promoting the HER and OER, and have been used for fabricating a novel hydroelectric generator to harvest the energy in water. Moreover, borophene and its heterostructures have shown excellent sensing properties in humidity sensor, gas sensor, pressure sensor, and photodetector. Besides, the fabrication of nonvolatile borophene-based memory devices has also been achieved, which display a low set voltage, a high ON/OFF, good stability, and even broad light response. Therefore, we hope that this review of recent borophene-based applications in the field of energy, sensors and information storage will not only spark further exploration, but also inspire the research of borophene in other application fields. Nevertheless, issues and challenges also remain in the development of borophene-based applications, and several suggestions for future efforts in these fields are put forward:

(1) The quality of borophene-based materials is reviewed as a key factor to influence on the performance of their devices. Although a series of breakthroughs have been made in the experimental synthesis of borophene-based materials in recent years, it is still difficult to obtain stable borophene-based materials with large area, single crystal, and controllable thickness. In future experiments, it is worth exploring whether the crystallinity of borophene can be improved by further optimizing the current experimental conditions, such as selecting a more suitable growth substrate, finding a more rational boron source and investigating a more appropriate growth temperature. In addition, it is also expected to develop a facile and novel method for synthesizing high-quality borophene. The investigation of the stable and semiconducting α'-4H-borophene which was prepared by *in-situ* thermal decomposition method not only points out the direction for its large-scale preparation, but also paves the way for the development of new methods for its preparation. Thus, removing set thinking and blazing new trails for the experimental growth of borophene-based materials seem to be necessary.

(2) Borophene-based materials have shown promising application prospects in energy storage, energy conversion, and energy harvesting, but related research is still in its infancy. It is urgent that more efforts are devoted to optimizing their performance. In addition to realizing the high-quality borophene mentioned in (1), element doping has been theoretically predicted as another effective strategy for boosting its storage capacity and improving its electrocatalytic performance. It needs to be verified by further experiments. Moreover, because of their excellent chemical stability in strong acids and bases, some freestanding stable borophenes may be suitable candidates for electrocatalytic reactions. However, their activities are still unknown and should be further explored experimentally.

(3) Because α'-4H-borophene and its heterostructures have been experimentally investigated and demonstrated to have excellent humidity-sensing, gas-sensing, and pressure-sensing properties, it is anticipated for the borophenes with other phases and their heterostructures to further reveal their sensing performances in subsequent experiments. Furthermore, the reported humidity or gas sensors were fabricated by simple drop-coating method, which limited the exploration of the effect of thickness on sensing performances. Thus, it is expected to reveal the sensing performances of thickness-controllable borophene obtained on insulating substrates by CVD method. Although we first reported the pressure borophene sensor towards flexible electronics, its large-scale integration is still quite difficult, which is a prerequisite for its practical application. In addition, it is also urgent for exploring the combination of borophene with other flexible substrates for more functional novel applications. We hope that more disciplines can participate in the research to promote the development of borophene in the field of flexible electronics.

(4) Despite memory devices based on borophene and its heterostructures have been fabricated, there still are some challenges in performance enhancement and switching mechanism understanding. The current research mainly focuses on the fabrication of the non-volatile resistive memory devices based on borophene-based materials and does not pay much attention to the optimization of the device performances. Therefore, systematic investigations should be performed to optimize the device performances from these factors, including the choice of the electrode and its thickness, surface functionalization, and the use of different phases of borophene or its heterostructures as the active layer. Moreover, although the typical electrical switching behavior has been found in solution-processed borophenes, the intrinsic mechanism was rarely revealed. The understanding of the switching mechanism in the memory devices is of great significance for guiding the design of high-performance devices in the future. Besides, although the borophene-based memory devices have shown excellent memristive characteristics, most reports mainly concentrate on the performance exploration of a single device and do not focus on device integration. The investigation of the device integration is necessary for realizing the practical

application of the borophene-based information storage device.

(5) Theoretically, borophene-based materials have also shown other excellent properties, such as superconductivity, ultrahigh carrier mobility, and ultrahigh thermal conductivity, which play an important role in advanced high-performance electronic information devices. Therefore, more efforts should be made to design the related experiment to verify the predicted results. Furthermore, the corresponding devices based on the properties are also anticipated to be fabricated in subsequent experiments. More importantly, with the successful realization of the borophene-based devices in various fields, a system which is entirely composed of borophene-based devices seems to be possible in the future.

Acknowledgements

This work was supported by the National Natural Science Foundation of China (No. 61774085), Natural Science Foundation of Jiangsu Province (No. BK20201300), the Research Fund of State Key Laboratory of Mechanics and Control of Mechanical Structures (Nanjing University of Aeronautics and Astronautics (NUAA)) (No. MCMS-I-0420G02), the Fundamental Research Funds for the Central Universities (No. NP2022401), the Fund of Prospective Layout of Scientific Research for NUAA (No. ILA22009), the Priority Academic Program Development of Jiangsu Higher Education Institutions, the Funding for Outstanding Doctoral Dissertation in NUAA (No. BCXJ22-02), the Interdisciplinary Innovation Fund for Doctoral Students of Nanjing University of Aeronautics and Astronautics (No. KXKCXJJ202201), and the Postgraduate Research & Practice Innovation Program of Jiangsu Province (No. KYCX22_0329).

Declaration of conflicting interest

The authors declare no conflicting interests regarding the content of this article.

References

[1] Novoselov, K. S.; Geim, A. K.; Morozov, S. V.; Jiang, D.; Zhang, Y.; Dubonos, S. V.; Grigorieva, I. V.; Firsov, A. A. Electric field effect in atomically thin carbon films. *Science* **2004**, *306*, 666–669.

[2] Geim, A. K. Graphene: Status and prospects. *Science* **2009**, *324*, 1530–1534.

[3] Chen, X. Y.; Fan, K.; Liu, Y.; Li, Y.; Liu, X. Y.; Feng, W.; Wang, X. Recent advances in fluorinated graphene from synthesis to applications: Critical review on functional chemistry and structure engineering. *Adv. Mater.* **2022**, *34*, 2101665.

[4] Urso, M.; Ussia, M.; Novotný, F.; Pumera, M. Trapping and detecting nanoplastics by MXene-derived oxide microrobots. *Nat. Commun.* **2022**, *13*, 3573.

[5] Mayorga-Burrezo, P.; Muñoz, J.; Zaoralová, D.; Otyepka, M.; Pumera, M. Multiresponsive 2D $Ti_3C_2T_x$ MXene via implanting molecular properties. *ACS Nano* **2021**, *15*, 10067–10075.

[6] Vaghasiya, J. V.; Mayorga-Martinez, C. C.; Vyskočil, J.; Sofer, Z.; Pumera, M. Integrated biomonitoring sensing with wearable asymmetric supercapacitors based on Ti_3C_2 MXene and 1T-phase WS_2 nanosheets. *Adv. Funct. Mater.* **2020**, *30*, 2003673.

[7] Chia, H. L.; Mayorga-Martinez, C. C.; Antonatos, N.; Sofer, Z.; Gonzalez-Julian, J. J.; Webster, R. D.; Pumera, M. MXene titanium carbide-based biosensor: Strong dependence of exfoliation method on performance. *Anal. Chem.* **2020**, *92*, 2452–2459.

[8] Chhowalla, M.; Liu, Z. F.; Zhang, H. Two-dimensional transition metal dichalcogenide (TMD) nanosheets. *Chem. Soc. Rev.* **2015**, *44*, 2584–2586.

[9] Yin, X. M.; Tang, C. S.; Zheng, Y.; Gao, J.; Wu, J.; Zhang, H.; Chhowalla, M.; Chen, W.; Wee, A. T. S. Recent developments in 2D transition metal dichalcogenides: Phase transition and applications of the (quasi-)metallic phases. *Chem. Soc. Rev.* **2021**, *50*, 10087–10115.

[10] Chen, T. A.; Chuu, C. P.; Tseng, C. C.; Wen, C. K.; Wong, H. S. P.; Pan, S. Y.; Li, R. T.; Chao, T. A.; Chueh, W. C.; Zhang, Y. F. et al. Wafer-scale single-crystal hexagonal boron nitride monolayers on Cu (111). *Nature* **2020**, *579*, 219–223.

[11] Kumar, R.; Sahoo, S.; Joanni, E.; Singh, R. K.; Yadav, R. M.; Verma, R. K.; Singh, D. P.; Tan, W. K.; Del Pino, A. P.; Moshkalev, S. A. et al. A review on synthesis of graphene, h-BN, and MoS_2 for energy storage applications: Recent progress and perspectives. *Nano Res.* **2019**, *12*, 2655–2694.

[12] Li, L. K.; Yu, Y. J.; Ye, G. J.; Ge, Q. Q.; Ou, X. D.; Wu, H.; Feng, D. L.; Chen, X. H.; Zhang, Y. B. Black phosphorus field-effect transistors. *Nat. Nanotechnol.* **2014**, *9*, 372–377.

[13] Vaghasiya, J. V.; Křípalová, K.; Hermanová, S.; Mayorga-Martinez, C. C.; Pumera, M. Real-time biomonitoring device based on 2D black phosphorus and polyaniline nanocomposite flexible supercapacitors. *Small* **2021**, *17*, 2102337.

[14] Qiu, M.; Ren, W. X.; Jeong, T.; Won, M.; Park, G. Y.; Sang, D. K.; Liu, L. P.; Zhang, H.; Kim, J. S. Omnipotent phosphorene: A next-generation, two-dimensional nanoplatform for multidisciplinary biomedical applications. *Chem. Soc. Rev.* **2018**, *47*, 5588–5601.

[15] Gusmao, R.; Sofer, Z.; Pumera, M. Black phosphorus rediscovered: From bulk material to monolayers. *Angew. Chem., Int. Ed.* **2017**, *56*, 8052–8072.

[16] Ng, S.; Sturala, J.; Vyskocil, J.; Lazar, P.; Martincova, J.; Plutnar, J.; Pumera, M. Two-dimensional functionalized germananes as photoelectrocatalysts. *ACS Nano* **2021**, *15*, 11681–11693.

[17] Chia, H. L.; Sturala, J.; Webster, R. D.; Pumera, M. Functionalized 2D germanene and silicene enzymatic system. *Adv. Funct. Mater.* **2021**, *31*, 2011125.

[18] Maric, T.; Beladi-Mousavi, S. M.; Khezri, B.; Sturala, J.; Nasir, M. Z. M.; Webster, R. D.; Sofer, Z.; Pumera, M. Functional 2D germanene fluorescent coating of microrobots for micromachines multiplexing. *Small* **2020**, *16*, 1902365.

[19] Muñoz, J.; Palacios-Corella, M.; Gómez, I. J.; Zajíčková, L.; Pumera, M. Synthetic nanoarchitectonics of functional organic–inorganic 2D germanane heterostructures via click chemistry. *Adv. Mater.* **2022**, *34*, 2206382.

[20] Rosli, N. F.; Rohaizad, N.; Sturala, J.; Fisher, A. C.; Webster, R. D.; Pumera, M. Siloxene, germanane, and methylgermanane: Functionalized 2D materials of group 14 for electrochemical applications. *Adv. Funct. Mater.* **2020**, *30*, 1910186.

[21] Piazza, Z. A.; Hu, H. S.; Li, W. L.; Zhao, Y. F.; Li, J.; Wang, L. S. Planar hexagonal B_{36} as a potential basis for extended single-atom layer boron sheets. *Nat. Commun.* **2014**, *5*, 3113.

[22] Sergeeva, A. P.; Popov, I. A.; Piazza, Z. A.; Li, W. L.; Romanescu, C.; Wang, L. S.; Boldyrev, A. I. Understanding boron through size-selected clusters: Structure, chemical bonding, and fluxionality. *Acc. Chem. Res.* **2014**, *47*, 1349–1358.

[23] Zhang, Z. H.; Penev, E. S.; Yakobson, B. I. Two-dimensional boron: Structures, properties and applications. *Chem. Soc. Rev.* **2017**, *46*, 6746–6763.

[24] Mannix, A. J.; Zhang, Z. H.; Guisinger, N. P.; Yakobson, B. I.; Hersam, M. C. Borophene as a prototype for synthetic 2D materials development. *Nat. Nanotechnol.* **2018**, *13*, 444–450.

[25] Sun, X.; Liu, X. F.; Yin, J.; Yu, J.; Li, Y.; Hang, Y.; Zhou, X. C.; Yu, M. L.; Li, J. D.; Tai, G. A. et al. Two-dimensional boron crystals: Structural stability, tunable properties, fabrications and applications. *Adv. Funct. Mater.* **2017**, *27*, 1603300.

[26] Zhang, Z. H.; Penev, E. S.; Yakobson, B. I. Polyphony in B flat. *Nat. Chem.* **2016**, *8*, 525–527.

[27] Tai, G. A.; Hu, T. S.; Zhou, Y. G.; Wang, X. F.; Kong, J. Z.; Zeng, T.; You, Y. C.; Wang, Q. Synthesis of atomically thin boron films on copper foils. *Angew. Chem., Int. Ed.* **2015**, *54*, 15473–15477.

[28] Mannix, A. J.; Zhou, X. F.; Kiraly, B.; Wood, J. D.; Alducin, D.; Myers, B. D.; Liu, X. L.; Fisher, B. L.; Santiago, U.; Guest, J. R. et al. Synthesis of borophenes: Anisotropic, two-dimensional boron polymorphs. *Science* **2015**, *350*, 1513–1516.
[29] Feng, B. J.; Zhang, J.; Zhong, Q.; Li, W. B.; Li, S.; Li, H.; Cheng, P.; Meng, S.; Chen, L.; Wu, K. H. Experimental realization of two-dimensional boron sheets. *Nat. Chem*. **2016**, *8*, 563–568.
[30] Xie, S. Y.; Wang, Y. L.; Li, X. B. Flat boron: A new cousin of graphene. *Adv. Mater*. **2019**, *31*, 1900392.
[31] Liu, L. R.; Zhang, Z. H.; Liu, X. L.; Xuan, X. Y.; Yakobson, B. I.; Hersam, M. C.; Guo, W. L. Borophene concentric superlattices via self-assembly of twin boundaries. *Nano Lett*. **2020**, *20*, 1315–1321.
[32] Penev, E. S.; Kutana, A.; Yakobson, B. I. Can Two-dimensional boron superconduct?. *Nano Lett*. **2016**, *16*, 2522–2526.
[33] Hou, C.; Tai, G. A.; Wu, Z. H.; Hao, J. Q. Borophene: Current status, challenges and opportunities. *ChemPlusChem* **2020**, *85*, 2186–2196.
[34] Kaneti, Y. V.; Benu, D. P.; Xu, X. T.; Yuliarto, B.; Yamauchi, Y.; Golberg, D. Borophene: Two-dimensional boron monolayer: Synthesis, properties, and potential applications. *Chem. Rev*. **2022**, *122*, 1000–1051.
[35] Nasir, M. Z. M.; Pumera, M. Emerging mono-elemental 2D nanomaterials for electrochemical sensing applications: From borophene to bismuthene. *TrAC Trends Anal. Chem*. **2019**, *121*, 115696.
[36] Wu, X. J.; Dai, J.; Zhao, Y.; Zhuo, Z. W.; Yang, J. L.; Zeng, X. C. Two-dimensional boron monolayer sheets. *ACS Nano* **2012**, *6*, 7443–7453.
[37] Hou, C.; Tai, G. A.; Hao, J. Q.; Sheng, L. H.; Liu, B.; Wu, Z. T. Ultrastable crystalline semiconducting hydrogenated borophene. *Angew. Chem., Int. Ed*. **2020**, *59*, 10819–10825.
[38] Wu, Z. H.; Tai, G. A.; Shao, W.; Wang, R.; Hou, C. Experimental realization of quasicubic boron sheets. *Nanoscale* **2020**, *12*, 3787–3794.
[39] Wu, Z. H.; Tai, G. A.; Liu, R. S.; Hou, C.; Shao, W.; Liang, X. C.; Wu, Z. T. Van der Waals epitaxial growth of borophene on a mica substrate toward a high-performance photodetector. *ACS Appl. Mater. Interfaces* **2021**, *13*, 31808–31815.
[40] Wu, Z. H.; Tai, G. A.; Liu, R. S.; Shao, W.; Hou, C.; Liang, X. C. Synthesis of borophene on quartz towards hydroelectric generators. *J. Mater. Chem. A* **2022**, *10*, 8218–8226.
[41] Tai, G. A.; Xu, M. P.; Hou, C.; Liu, R. S.; Liang, X. C.; Wu, Z. T. Borophene nanosheets as high-efficiency catalysts for the hydrogen evolution reaction. *ACS Appl. Mater. Interfaces* **2021**, *13*, 60987–60994.
[42] Jiang, H. R.; Lu, Z. H.; Wu, M. C.; Ciucci, F.; Zhao, T. S. Borophene: A promising anode material offering high specific capacity and high rate capability for lithium-ion batteries. *Nano Energy* **2016**, *23*, 97–104.
[43] Huang, T. H.; Tian, B. W.; Guo, J. Y.; Shu, H. B.; Wang, Y.; Dai, J. Semiconducting borophene as a promising anode material for Li-ion and Na-ion batteries. *Mater. Sci. Semicond. Process*. **2019**, *89*, 250–255.
[44] Cheng, T.; Lang, H. F.; Li, Z. Z.; Liu, Z. F.; Liu, Z. R. Anisotropic carrier mobility in two-dimensional materials with tilted Dirac cones: Theory and application. *Phys. Chem. Chem. Phys*. **2017**, *19*, 23942–23950.
[45] Zhang, J. J.; Altalhi, T.; Yang, J. H.; Yakobson, B. I. Semiconducting α'-boron sheet with high mobility and low all-boron contact resistance: A first-principles study. *Nanoscale* **2021**, *13*, 8474–8480.
[46] Shen, J. L.; Yang, Z.; Wang, Y. T.; Xu, L. C.; Liu, R. P.; Liu, X. G. The gas sensing performance of borophene/MoS_2 heterostructure. *Appl. Surf. Sci*. **2020**, *504*, 144412.
[47] Shukla, V.; Wärnå, J.; Jena, N. K.; Grigoriev, A.; Ahuja, R. Toward the realization of 2D borophene based gas sensor. *J. Phys. Chem. C* **2017**, *121*, 26869–26876.
[48] Nagarajan, V.; Chandiramouli, R. Borophene nanosheet molecular device for detection of ethanol-a first-principles study. *Comput. Theor. Chem*. **2017**, *1105*, 52–60.
[49] Huang, C. S.; Murat, A.; Babar, V.; Montes, E.; Schwingenschlögl, U. Adsorption of the gas molecules NH_3, NO, NO_2, and CO on borophene. *J. Phys. Chem. C* **2018**, *122*, 14665–14670.
[50] Chen, Y. L.; Yu, G. T.; Chen, W.; Liu, Y. P.; Li, G. D.; Zhu, P. W.; Tao, Q.; Li, Q. J.; Liu, J. W.; Shen, X. P. et al. Highly active, nonprecious electrocatalyst comprising borophene subunits for the hydrogen evolution reaction. *J. Am. Chem. Soc*. **2017**, *139*, 12370–12373.
[51] Shi, L.; Ling, C. Y.; Ouyang, Y. X.; Wang, J. L. High intrinsic catalytic activity of two-dimensional boron monolayers for the hydrogen evolution reaction. *Nanoscale* **2017**, *9*, 533–537.
[52] Li, H. L.; Jing, L.; Liu, W. W.; Lin, J. J.; Tay, R. Y.; Tsang, S. H.; Teo, E. H. T. Scalable production of few-layer boron sheets by liquid-phase exfoliation and their superior supercapacitive performance. *ACS Nano* **2018**, *12*, 1262–1272.
[53] Chahal, S.; Ranjan, P.; Motlag, M.; Yamijala, S. S. R. K. C.; Late, D. J.; Sadki, E. H. S.; Cheng, G. J.; Kumar, P. Borophene via micromechanical exfoliation. *Adv. Mater*. **2021**, *33*, 2102039.
[54] Liang, X. C.; Hao, J. Q.; Zhang, P. Y.; Hou, C.; Tai, G. A. Freestanding α-rhombohedral borophene nanosheets: Preparation and memory device application. *Nanotechnology* **2022**, *33*, 505601.
[55] Abdi, Y.; Mazaheri, A.; Hajibaba, S.; Darbari, S.; Rezvani, S. J.; Cicco, A. D.; Paparoni, F.; Rahighi, R.; Gholipour, S.; Rashidi, A. et al. A two-dimensional borophene supercapacitor. *ACS Materials Lett*. **2022**, *4*, 1929–1936.
[56] Ranjan, P.; Sahu, T. K.; Bhushan, R.; Yamijala, S. S. R. K. C.; Late, D. J.; Kumar, P.; Vinu, A. Freestanding borophene and its hybrids. *Adv. Mater*. **2019**, *31*, 1900353.
[57] Hou, C.; Tai, G. A.; Liu, B.; Wu, Z. H.; Yin, Y. H. Borophene–graphene heterostructure: Preparation and ultrasensitive humidity sensing. *Nano Res*. **2021**, *14*, 2337–2344.
[58] Hou, C.; Tai, G. A.; Liu, Y.; Wu, Z. T.; Wu, Z. H.; Liang, X. C. Ultrasensitive humidity sensing and the multifunctional applications of borophene–MoS_2 heterostructures. *J. Mater. Chem. A* **2021**, *9*, 13100–13108.
[59] Tai, G. A.; Liu, B.; Hou, C.; Wu, Z. T.; Liang, X. C. Ultraviolet photodetector based on p-borophene/n-ZnO heterojunction. *Nanotechnology* **2021**, *32*, 505606.
[60] Liu, R. S.; Hou, C.; Liang, X. C.; Wu, Z. T.; Tai, G. A. Borophene–ZnO heterostructures: Preparation and application as broadband photonic nonvolatile memory. *Nano Res*., in press, DOI: 10.1007/s12274-022-5185-6.
[61] Wu, Z. T.; Yin, Y. H.; Hou, C.; Tai, G. A. Borophene reinforcing copper matrix composites: Preparation and mechanical properties. *J. Alloys Compd*. **2023**, *930*, 167370.
[62] Lin, H. J.; Shi, H. D.; Wang, Z.; Mu, Y. W.; Li, S. D.; Zhao, J. J.; Guo, J. W.; Yang, B.; Wu, Z. S.; Liu, F. Scalable production of freestanding few-layer β_{12}-borophene single crystalline sheets as efficient electrocatalysts for lithium-sulfur batteries. *ACS Nano* **2021**, *15*, 17327–17336.
[63] Ding, J. W.; Zheng, H. Y.; Wang, S. W.; Ji, X. Y. Hydrogenated borophene nanosheets based multifunctional quasi-solid-state electrolytes for lithium metal batteries. *J. Colloid Interfacs Sci*. **2022**, *615*, 79–86.
[64] Wang, X. F.; Tai, G. A.; Wu, Z. H.; Hu, T. S.; Wang, R. Ultrathin molybdenum boride films for highly efficient catalysis of the hydrogen evolution reaction. *J. Mater. Chem. A* **2017**, *5*, 23471–23475.
[65] Xu, M. P.; Wang, R.; Bian, K.; Hou, C.; Wu, Y. X.; Tai, G. A. Triclinic boron nanosheets high-efficient electrocatalysts for water splitting. *Nanotechnology* **2022**, *33*, 075601.
[66] Chen, K.; Wang, Z. M.; Wang, L.; Wu, X. Z.; Hu, B. J.; Liu, Z.; Wu, M. H. Boron nanosheet-supported Rh catalysts for hydrogen

evolution: A new territory for the strong metal–support interaction effect. *Nano-Micro Lett*. **2021**, *13*, 138.

[67] Saad, A.; Liu, D. Q.; Wu, Y. C.; Song, Z. Q.; Li, Y.; Najam, T.; Zong, K.; Tsiakaras, P.; Cai, X. K. Ag nanoparticles modified crumpled borophene supported Co_3O_4 catalyst showing superior oxygen evolution reaction (OER) performance. *Appl*. *Catal*. *B*: *Environ*. **2021**, *298*, 120529.

[68] Hou, C.; Tai, G. A.; Liu, Y.; Liu, X. Borophene gas sensor. *Nano Res*. **2022**, *15*, 2537–2544.

[69] Hou, C.; Tai, G. A.; Liu, Y.; Liu, R. S.; Liang, X. C.; Wu, Z. T.; Wu, Z. H. Borophene pressure sensing for electronic skin and human–machine interface. *Nano Energy* **2022**, *97*, 107189.

[70] Ma, D. T.; Wang, R.; Zhao, J. L.; Chen, Q. Y.; Wu, L. M.; Li, D. L.; Su, L. M.; Jiang, X. T.; Luo, Z. Q.; Ge, Y. Q. et al. A self-powered photodetector based on two-dimensional boron nanosheets. *Nanoscale* **2020**, *12*, 5313–5323.

[71] Shao, W.; Tai, G. A.; Hou, C.; Wu, Z. H.; Wu, Z. T.; Liang, X. C. Borophene-functionalized magnetic nanoparticles: Synthesis and memory device application. *ACS Appl*. *Electron*. *Mater*. **2021**, *3*, 1133–1141.

[72] Boustani, I. Systematic *ab initio* investigation of bare boron clusters: mDetermination of the geometryand electronic structures of B_n (n = 2–14). *Phys*. *Rev*. *B* **1997**, *55*, 16426–16438.

[73] Szwacki, N. G.; Sadrzadeh, A.; Yakobson, B. I. B_{80} fullerene: An *ab initio* prediction of geometry, stability, and electronic structure. *Phys*. *Rev*. *Lett*. **2007**, *98*, 166804.

[74] Tang, H.; Ismail-Beigi, S. Novel precursors for boron nanotubes: The competition of two-center and three-center bonding in boron sheets. *Phys*. *Rev*. *Lett*. **2007**, *99*, 115501.

[75] Yang, X. B.; Ding, Y.; Ni, J. *Ab initio* prediction of stable boron sheets and boron nanotubes: Structure, stability, and electronic properties. *Phys*. *Rev*. *B* **2008**, *77*, 041402.

[76] Penev, E. S.; Artyukhov, V. I.; Ding, F.; Yakobson, B. I. Unfolding the fullerene: Nanotubes, graphene and poly-elemental varieties by simulations. *Adv*. *Mater*. **2012**, *24*, 4956–4976.

[77] Liu, Y. Y.; Penev, E. S.; Yakobson, B. I. Probing the synthesis of two-dimensional boron by first-principles computations. *Angew*. *Chem*., *Int*. *Ed*. **2013**, *52*, 3156–3159.

[78] Penev, E. S.; Bhowmick, S.; Sadrzadeh, A.; Yakobson, B. I. Polymorphism of two-dimensional boron. *Nano Lett*. **2012**, *12*, 2441–2445.

[79] Zhang, Z. H.; Yang, Y.; Gao, G. Y.; Yakobson, B. I. Two-dimensional boron monolayers mediated by metal substrates. *Angew*. *Chem*., *Int*. *Ed*. **2015**, *54*, 13022–13026.

[80] Zhang, Z. H.; Mannix, A. J.; Liu, X. L.; Hu, Z. L.; Guisinger, N. P.; Hersam, M. C.; Yakobson, B. I. Near-equilibrium growth from borophene edges on silver. *Sci*. *Adv*. **2019**, *5*, eaax0246.

[81] Jiao, Y. L.; Ma, F. X.; Bell, J.; Bilic, A.; Du, A. J. Two-dimensional boron hydride sheets: High stability, massless dirac fermions, and excellent mechanical properties. *Angew*. *Chem*., *Int*. *Ed*. **2016**, *55*, 10292–10295.

[82] Kou, L. Z.; Ma, Y. D.; Tang, C.; Sun, Z. Q.; Du, A. J.; Chen, C. F. Auxetic and ferroelastic borophane: A novel 2D material with negative Possion's ratio and switchable dirac transport channels. *Nano Lett*. **2016**, *16*, 7910–7914.

[83] Wang, Z. Q.; Lü, T. Y.; Wang, H. Q.; Feng, Y. P.; Zheng, J. C. High anisotropy of fully hydrogenated borophene. *Phys*. *Chem*. *Chem*. *Phys*. **2016**, *18*, 31424–31430.

[84] Xu, Y.; Zhang, P. K.; Xuan, X. Y.; Xue, M. M.; Zhang, Z. H.; Guo, W. L.; Yakobson, B. I. Borophane polymorphs. *J*. *Phys*. *Chem*. *Lett*. **2022**, *13*, 1107–1113.

[85] Xu, Y.; Xuan, X. Y.; Yang, T. F.; Zhang, Z. H.; Li, S. D.; Guo, W. L. Quasi-freestanding bilayer borophene on Ag(111). *Nano Lett*. **2022**, *22*, 3488–3494.

[86] Li, W. B.; Kong, L. J.; Chen, C. Y.; Gou, J.; Sheng, S. X.; Zhang, W. F.; Li, H.; Chen, L.; Cheng, P.; Wu, K. H. Experimental realization of honeycomb borophene. *Sci*. *Bull*. **2018**, *63*, 282–286.

[87] Wu, R. T.; Drozdov, I. K.; Eltinge, S.; Zahl, P.; Ismail-Beigi, S.; Božović, I.; Gozar, A. Large-area single-crystal sheets of borophene on Cu(111) surfaces. *Nat*. *Nanotechnol*. **2019**, *14*, 44–49.

[88] Kiraly, B.; Liu, X. L.; Wang, L. Q.; Zhang, Z. H.; Mannix, A. J.; Fisher, B. L.; Yakobson, B. I.; Hersam, M. C.; Guisinger, N. P. Borophene synthesis on Au(111). *ACS Nano* **2019**, *13*, 3816–3822.

[89] Vinogradov, N. A.; Lyalin, A.; Taketsugu, T.; Vinogradov, A. S.; Preobrajenski, A. Single-phase borophene on Ir(111): Formation, structure, and decoupling from the support. *ACS Nano* **2019**, *13*, 14511–14518.

[90] Omambac, K. M.; Petrović, M.; Bampoulis, P.; Brand, C.; Kriegel, M. A.; Dreher, P.; Janoschka, D.; Hagemann, U.; Hartmann, N.; Valerius, P. et al. Segregation-enhanced epitaxy of borophene on Ir(111) by thermal decomposition of borazine. *ACS Nano* **2021**, *15*, 7421–7429.

[91] Nishino, H.; Fujita, T.; Cuong, N. T.; Tominaka, S.; Miyauchi, M.; Iimura, S.; Hirata, A.; Umezawa, N.; Okada, S.; Nishibori, E. et al. Formation and characterization of hydrogen boride sheets derived from MgB_2 by cation exchange. *J*. *Am*. *Chem*. *Soc*. **2017**, *139*, 13761–13769.

[92] Kawamura, R.; Cuong, N. T.; Fujita, T.; Ishibiki, R.; Hirabayashi, T.; Yamaguchi, A.; Matsuda, I.; Okada, S.; Kondo, T.; Miyauchi, M. Photoinduced hydrogen release from hydrogen boride sheets. *Nat*. *Commun*. **2019**, *10*, 4880.

[93] Tao, Y. Q.; Wang, Q.; Ji, S. S.; Wang, Y.; Zhou, Q. Y.; Huang, Z. D.; Li, H.; Huang, X.; Chen, B.; Li, S. Z. A solvent decomposition and explosion approach for boron nanoplate synthesis. *Chem*. *Commun*. **2021**, *57*, 4922–4925.

[94] Li, Q. C.; Kolluru, V. S. C.; Rahn, M. S.; Schwenker, E.; Li, S. W.; Hennig, R. G.; Darancet, P.; Chan, M. K. Y.; Hersam, M. C. Synthesis of borophane polymorphs through hydrogenation of borophene. *Science* **2021**, *371*, 1143–1148.

[95] Liu, X. L.; Hersam, M. C. Borophene–graphene heterostructures. *Sci*. *Adv*. **2019**, *5*, eaax6444.

[96] Li, Q. C.; Liu, X. L.; Aklile, E. B.; Li, S. W.; Hersam, M. C. Self-assembled borophene/graphene nanoribbon mixed-dimensional heterostructures. *Nano Lett*. **2021**, *21*, 4029–4035.

[97] Liu, X. L.; Li, Q. C.; Ruan, Q. Y.; Rahn, M. S.; Yakobson, B. I.; Hersam, M. C. Borophene synthesis beyond the single-atomic-layer limit. *Nat*. *Mater*. **2022**, *21*, 35–40.

[98] Chen, C. Y.; Lv, H. F.; Zhang, P.; Zhuo, Z. W.; Wang, Y.; Ma, C.; Li, W. B.; Wang, X. G.; Feng, B. J.; Cheng, P. et al. Synthesis of bilayer borophene. *Nat*. *Chem*. **2022**, *14*, 25–31.

[99] Guo, X.; Wang, C. D.; Wang, W. J.; Zhou, Q.; Xu, W. J.; Zhang, P. J.; Wei, S. Q.; Cao, Y. Y.; Zhu, K. F.; Liu, Z. F. et al. Vacancy manipulating of molybdenum carbide MXenes to enhance Faraday reaction for high performance lithium-ion batteries. *Nano Res*. *Energy* **2022**, *1*, e9120026.

[100] Zhang, P. P.; Wang, F. X.; Yu, M. H.; Zhuang, X. D.; Feng, X. L. Two-dimensional materials for miniaturized energy storage devices: From individual devices to smart integrated systems. *Chem*. *Soc*. *Rev*. **2018**, *47*, 7426–7451.

[101] Ju, Z. Y.; Zhang, X.; Wu, J. Y.; Yu, G. H. Vertically aligned two-dimensional materials-based thick electrodes for scalable energy storage systems. *Nano Res*. **2021**, *14*, 3562–3575.

[102] Mendoza-Sánchez, B.; Gogotsi, Y. Synthesis of two-dimensional materials for capacitive energy storage. *Adv*. *Mater*. **2016**, *28*, 6104–6135.

[103] Liu, C. L.; Bai, Y.; Li, W. T.; Yang, F. Y.; Zhang, G. X.; Pang, H. *In situ* growth of three-dimensional MXene/metal–organic framework composites for high-performance supercapacitors. *Angew*. *Chem*., *Int*. *Ed*. **2022**, *61*, e202116282.

[104] Geng, P. B.; Wang, L.; Du, M.; Bai, Y.; Li, W. T.; Liu, Y. F.; Chen, S. Q.; Braunstein, P.; Xu, Q.; Pang, H. MIL-96-Al for Li-S batteries: Shape or size?. *Adv*. *Mater*. **2021**, *34*, 2107836.

[105] Chen, T. T.; Wang, F. F.; Cao, S.; Bai, Y.; Zheng, S. S.; Li, W. T.; Zhang, S. T.; Hu, S. X.; Pang, H. *In situ* synthesis of MOF-74

family for high areal energy density of aqueous nickel-zinc batteries. *Adv. Mater.* **2022**, *34*, 2201779.

[106] Zhu, J. Y.; Childress, A. S.; Karakaya, M.; Dandeliya, S.; Srivastava, A.; Lin, Y.; Rao, A. M.; Podila, R. Defect-engineered graphene for high-energy- and high-power-density supercapacitor devices. *Adv. Mater.* **2016**, *28*, 7185–7192.

[107] Shi, H. D.; Qin, J. Q.; Huang, K.; Lu, P. F.; Zhang, C. F.; Dong, Y. F.; Ye, M.; Liu, Z. M.; Wu, Z. S. A two-dimensional mesoporous polypyrrole–graphene oxide heterostructure as a dual-functional ion redistributor for dendrite-free lithium metal anodes. *Angew. Chem., Int. Ed.* **2020**, *59*, 12147–12153.

[108] Li, L.; Chen, L.; Mukherjee, S.; Gao, J.; Sun, H.; Liu, Z. B.; Ma, X. L.; Gupta, T.; Singh, C. V.; Ren, W. C. et al. Phosphorene as a polysulfide immobilizer and catalyst in high-performance lithium-sulfur batteries. *Adv. Mater.* **2017**, *29*, 1602734.

[109] Dong, Y. F.; Zheng, S. H.; Qin, J. Q.; Zhao, X. J.; Shi, H. D.; Wang, X. H.; Chen, J.; Wu, Z. S. All-MXene-based integrated electrode constructed by Ti_3C_2 nanoribbon framework host and nanosheet interlayer for high-energy-density Li-S batteries. *ACS Nano* **2018**, *12*, 2381–2388.

[110] Jiang, H. R.; Shyy, W.; Liu, M.; Ren, Y. X.; Zhao, T. S. Borophene and defective borophene as potential anchoring materials for lithium-sulfur batteries: A first-principles study. *J. Mater. Chem. A* **2018**, *6*, 2107–2114.

[111] Zhang, L.; Liang, P.; Shu, H. B.; Man, X. L.; Li, F.; Huang, J.; Dong, Q. M.; Chao, D. L. Borophene as efficient sulfur hosts for lithium-sulfur batteries: suppressing shuttle effect and improving conductivity. *J. Phys. Chem. C* **2017**, *121*, 15549–15555.

[112] Rao, D. W.; Zhang, L. Y.; Meng, Z. S.; Zhang, X. R.; Wang, Y. H.; Qiao, G. J.; Shen, X. Q.; Xia, H.; Liu, J. H.; Lu, R. F. Ultrahigh energy storage and ultrafast ion diffusion in borophene-based anodes for rechargeable metal ion batteries. *J. Mater. Chem. A* **2017**, *5*, 2328–2338.

[113] Chen, Y.; Zhang, X.; Zhang, D. C.; Yu, P.; Ma, Y. W. High performance supercapacitors based on reduced graphene oxide in aqueous and ionic liquid electrolytes. *Carbon* **2011**, *49*, 573–580.

[114] Lei, Z. B.; Liu, Z. H.; Wang, H. J.; Sun, X. X.; Lu, L.; Zhao, X. S. A high-energy-density supercapacitor with graphene-CMK-5 as the electrode and ionic liquid as the electrolyte. *J. Mater. Chem. A* **2013**, *1*, 2313–2321.

[115] Li, C.; Liu, B. W.; Jiang, N. Y.; Ding, Y. Elucidating the charge-transfer and Li-ion-migration mechanisms in commercial lithium-ion batteries with advanced electron microscopy. *Nano Res. Energy*, **2022**, *1*, e9120031.

[116] Liu, C. W.; Dai, Z. X.; Zhang, J.; Jin, Y. G.; Li, D. S.; Sun, C. H. Two-dimensional boron sheets as metal-free catalysts for hydrogen evolution reaction. *J. Phys. Chem. C* **2018**, *122*, 19051–19055.

[117] Xu, X. W.; Si, R. H.; Dong, Y.; Li, L. L.; Zhang, M. H.; Wu, X. Y.; Zhang, J.; Fu, K.; Guo, Y.; He, Y. Y. Borophene-supported single transition metal atoms as potential oxygen evolution/reduction electrocatalysts: A density functional theory study. *J. Mol. Model.* **2021**, *27*, 67.

[118] Singh, Y.; Back, S.; Jung, Y. Computational exploration of borophane-supported single transition metal atoms as potential oxygen reduction and evolution electrocatalysts. *Phys. Chem. Chem. Phys.* **2018**, *20*, 21095–21104.

[119] Gu, J. W.; Peng, Y.; Zhou, T.; Ma, J.; Pang, H.; Yamauchi, Y. Porphyrin-based framework materials for energy conversion. *Nano Res. Energy* **2022**, *1*, e9120009.

[120] Li, L.; Hu, L. P.; Li, J.; Wei, Z. D. Enhanced stability of Pt nanoparticle electrocatalysts for fuel cells. *Nano Res.* **2015**, *8*, 418–440.

[121] Yan, X. X.; Gu, M. Y.; Wang, Y.; Xu, L.; Tang, Y. W.; Wu, R. B. *In-situ* growth of Ni nanoparticle-encapsulated N-doped carbon nanotubes on carbon nanorods for efficient hydrogen evolution electrocatalysis. *Nano Res.* **2020**, *13*, 975–982.

[122] Zhang, Z.; Li, X. P.; Zhong, C.; Zhao, N. Q.; Deng, Y. D.; Han, X. P.; Hu, W. B. Spontaneous synthesis of silver-nanoparticle-decorated transition-metal hydroxides for enhanced oxygen evolution reaction. *Angew. Chem., Int. Ed.* **2020**, *59*, 7245–7250.

[123] Wang, X. F.; Lin, F. R.; Wang, X.; Fang, S. M.; Tan, J.; Chu, W. C.; Rong, R.; Yin, J.; Zhang, Z. H.; Liu, Y. P. et al. Hydrovoltaic technology: From mechanism to applications. *Chem. Soc. Rev.* **2022**, *51*, 4902–4927.

[124] Tang, W.; Chen, B. D.; Wang, Z. L. Recent progress in power generation from water/liquid droplet interaction with solid surfaces. *Adv. Funct. Mater.* **2019**, *29*, 1901069.

[125] Meng, Z.; Stolz, R. M.; Mendecki, L.; Mirica, K. A. Electrically-transduced chemical sensors based on two-dimensional nanomaterials. *Chem. Rev.* **2019**, *119*, 478–598.

[126] Liu, J.; Jiang, X. T.; Zhang, R. Y.; Zhang, Y.; Wu, L. M.; Lu, W.; Li, J. Q.; Li, Y. C.; Zhang, H. MXene-enabled electrochemical microfluidic biosensor: Applications toward multicomponent continuous monitoring in whole blood. *Adv. Funct. Mater.* **2019**, *29*, 1807326.

[127] Someya, T.; Amagai, M. Toward a new generation of smart skins. *Nat. Biotechnol.* **2019**, *37*, 382–388.

[128] Long, M. S.; Wang, P.; Fang, H. H.; Hu, W. D. Progress, challenges, and opportunities for 2D material based photodetectors. *Adv. Funct. Mater.* **2019**, *29*, 1803807.

[129] Bediako, D. K.; Rezaee, M.; Yoo, H.; Larson, D. T.; Zhao, S. Y. F.; Taniguchi, T.; Watanabe, K.; Brower-Thomas, T. L.; Kaxiras, E.; Kim, P. Heterointerface effects in the electrointercalation of van der Waals heterostructures. *Nature* **2018**, *558*, 425–429.

[130] Roy, K.; Padmanabhan, M.; Goswami, S.; Sai, T. P.; Ramalingam, G.; Raghavan, S.; Ghosh, A. Graphene–MoS_2 hybrid structures for multifunctional photoresponsive memory devices. *Nat. Nanotechnol.* **2013**, *8*, 826–830.

[131] Liu, X. L.; Wei, Z. H.; Balla, I.; Mannix, A. J.; Guisinger, N. P.; Luijten, E.; Hersam, M. C. Self-assembly of electronically abrupt borophene/organic lateral heterostructures. *Sci. Adv.* **2017**, *3*, e1602356.

[132] Popov, V. I.; Nikolaev, D. V.; Timofeev, V. B.; Smagulova, S. A.; Antonova, I. V. Graphene-based humidity sensors: The origin of alternating resistance change. *Nanotechnology* **2017**, *28*, 355501.

[133] Zhao, J.; Li, N.; Yu, H.; Wei, Z.; Liao, M. Z., Chen, P.; Wang, S. P.; Shi, D. X.; Sun, Q. J.; Zhang, G. Y. Highly sensitive MoS_2 humidity sensors array for noncontact sensation. *Adv. Mater.* **2017**, *29*, 1702076.

[134] Erande, M. B.; Pawar, M. S.; Late, D. J. Humidity sensing and photodetection behavior of electrochemically exfoliated atomically thin-layered black phosphorus nanosheets. *ACS Appl. Mater. Interfaces* **2016**, *8*, 11548–11556.

[135] Phan, D. T.; Park, I.; Park, A. R.; Park, C. M.; Jeon, K. J. Black P/graphene hybrid: A fast response humidity sensor with good reversibility and stability. *Sci. Rep.* **2017**, *7*, 10561.

[136] Tan, C. L.; Liu, Z. D.; Huang, W.; Zhang, H. Non-volatile resistive memory devices based on solution-processed ultrathin two-dimensional nanomaterials. *Chem. Soc. Rev.* **2015**, *44*, 2615–2628.

[137] Sebastian, A.; Le Gallo, M.; Khaddam-Aljameh, R.; Eleftheriou, E. Memory devices and applications for in-memory computing. *Nat. Nanotechnol.* **2020**, *15*, 529–544.

[138] Liu, J. Q.; Zeng, Z. Y.; Cao, X. H.; Lu, G.; Wang, L. H.; Fan, Q. L.; Huang, W.; Zhang, H. Preparation of MoS_2-polyvinylpyrrolidone nanocomposites for flexible nonvolatile rewritable memory devices with reduced graphene oxide electrodes. *Small* **2012**, *8*, 3517–3522.

[139] Zhang, P. Y.; Hou, C.; Shao, W.; Liu, R. S.; Wu, Z. T.; Tai, G. A. Crystalline BC_2N quantum dots. *Nano Res.*, in press, DOI: 10.1007/s12274-022-5284-4.

[140] Hao, J. Q.; Tai, G. A.; Zhou, J. X.; Wang, R.; Hou, C.; Guo, W. L. Crystalline semiconductor boron quantum dots. *ACS Appl. Mater. Interfaces* **2020**, *12*, 17669–17675.

Chuang Hou received his Bachelor's degree from North University of China in 2018. He is currently a Ph.D. candidate in Prof. Guoan Tai's group. His research focuses on the synthesis and device application of borophene.

Prof. Guoan Tai received his Ph.D. from Nanjing University of Aeronautics and Astronautics, and was a Postdoctoral Fellow in Department of Applied Physics at The Hong Kong Polytechnic University. He is currently a full professor in College of Aerospace Engineering at Nanjing University of Aeronautics and Astronautics. His research interests focus on the photodetectors and sensors based on 2D materials, energy storage and conversion devices.